The microtubule organization in the zebrafish yolk adapts to transgene-mediated phenotypic variations

Maria Marsal[+], Matteo Bernardello[+], Emilio J. Gualda[+] and Pablo Loza-Alvarez[*]

ICFO-Institut de Ciencies Fotoniques, The Barcelona Institute of Science and Technology, Castelldefels, Barcelona, Spain

[+]Contributed equally

[*]Correspondence: pablo.loza@icfo.eu

SUMMARY

The organization of microtubule networks in the cells is orchestrated by subcellular structures named microtubule organizing centers (MTOCs). In zebrafish embryos, the yolk is surrounded by a cytoplasmic layer containing a vast network of microtubules. In order to understand how this complex network is organized, we use dclk2-GFP zebrafish embryos, as a microtubule reporter line, and Light Sheet Fluorescence Microscopy. We find that this organization is mediated by a variable number of aster-like MTOCs during epiboly, and that it does not follow a rigid scheme, exemplifying developmental robustness. We characterize asters morphology, dynamics, and their uniform distribution in the yolk sphere. Consistent with their role as MTOCs we find that they contain key molecular machinery for MTs dynamics, amongst which centrin marks the assignation of MTOCs over time. Finally, we demonstrate that merely the overexpression of dclk2-GFP in wild type embryos can induce the formation of asters. We propose dclk2-GFP embryos as a model for the study of the collective behaviour of microtubules in complex systems.

INTRODUCTION

Epiboly is one of the cell movements of gastrulation, highly conserved throughout evolution. It consists of the thinning and spreading of different cell layers over and around the yolk cell (Betchaku and Trinkaus, 1978; Warga and Kimmel, 1990). In zebrafish, after fertilization, meroblastic cleavages give rise to the blastoderm, sitting on top of the big yolk cell that does not divide. After the 9th or 10th division cycle, the more marginal blastoderm cells release their cell contents into the yolk, forming a syncytium (Chu *et al.*, 2012). This is named the yolk syncytial layer (YSL), which is adjacent to a thin cytoplasmic layer (YCL) that wraps the viscous yolk mainly composed of lipid granules (Kimmel and Law, 1985; Kimmel *et al.*, 1995; Carvalho and Heisenberg, 2010). The nuclei of the YSL (YSN) undergo three rounds of divisions and become post-mitotic (Kane, Warga and Kimmel, 1992). Soon after that, some YSN move underneath the blastoderm (internal-YSN, i-YSN) and others stay at the surface (external-YSN, e-YSN) and undergo epiboly together with the blastoderm (D'Amico and Cooper, 2001; Carvalho *et al.*, 2009). Acto-myosin motors in the YSL and a polarized gradient of cortical tension are currently seen as the driving epiboly motors (Cheng, Miller and Webb, 2004; Köppen *et al.*, 2006; Behrndt *et al.*, 2012; Bruce, 2016; Hernández-Vega *et al.*, 2017).

It is known, that the zebrafish YSL and YCL contain microtubule (MT) networks that undergo various changes (MT density, MT length) over the different developmental stages (Solnica-Krezel and Driever, 1994; Jesuthasan and Strähle, 1997; Tran *et al.*, 2012; Eckerle *et al.*, 2018). However, during embryogenesis, little is known about the specific mechanisms that pattern such a network. In general, the organization of MTs is not random but is orchestrated by defined subcellular regions called MT organizing centers (MTOCs). Often, the MTs are organized in a radial way, nucleated from a central organizing region, forming what it is known as a MT aster. This is how the centrosomes, used by dividing animal cells, organize the mitotic spindle. The best-studied MTOC is the centrosome but it has further been shown that differentiated cells can generate alternative MT organizations through the reassignment of MTOC functions to non-centrosomal sites in interphase cells. These non-centrosomal MTOCs (nc-MTOCs) often serve as mechanical support or intracellular transport scaffolds (Sanchez and Feldman, 2017).

In zebrafish, yolk cell MTs are necessary for the migration of the e-YSN (Solnica-Krezel and Driever, 1994; Fei *et al.*, 2019). However, their role, either instructive or permissive is not yet fully understood. Yolk cell MTs are sensitive to environmental conditions (Strahle and Jesuthasan, 1993; Jesuthasan and Strähle, 1997; Sarmah *et al.*, 2013) and the defects in the yolk MT network are often seen in epiboly mutants. However, it is difficult to know if the MT defects are the primary cause of the phenotype (Du et al., 2012; (Li-Villarreal *et al.*, 2015; Eckerle *et al.*, 2018). Not only the function but also the arrangement of the MT network in the zebrafish yolk cell is not yet completely understood. This is because the problem has been approached only partially, both in time and in space. In fact, the primary approach has been immunostaining on fixed samples (Strahle and Jesuthasan, 1993; Topczewski and Solnica-Krezel, 1999), thus, hiding the rich variety of phenotypes over time and its dynamic nature. Only recently, the use of reporter transgenic lines and laser scanning confocal

microscopy allowed the dynamical study of yolk cell MTs, although only in restricted areas and in a limited time window (Tran *et al.*, 2012; Eckerle *et al.*, 2018; Fei *et al.*, 2019).

In this work, we use Light-Sheet Fluorescence Microscopy (LSFM), Laser Scanning Confocal Microscopy (LSCM) and the MT reporter line Tg(Xla.Eef1a1:dclk2a-GFP) (Tran *et al.*, 2012) to obtain a mesoscopic description of the spatio-temporal yolk cell MT organization during early zebrafish development and to find out the cellular and molecular mechanism responsible of building this network.

Thanks to the high-throughput capabilities of our custom-made LSFM microscope we are now able to quantitatively assess the high phenotypic variability of yolk MT organization. Thus, in addition to confirming the existence of previously reported MTOCs in the YSL (Solnica-Krezel and Driever, 1994; Fei *et al.*, 2019) we provide new insights on the mesoscopic description of the yolk MT organization and identify, at middle-stage epiboly and for the first time, the presence of MTOCs in the YCL. Here, we perform a thorough analysis of this newly find yolk MT network organization. We find that the YCL MTOCs appear regularly in a precise time window occupying the yolk surface, and assemble into large 3D patterns of radially oriented MT (YCL asters). We analyze their spatial dimensions and microns-scale architecture and hypothesize on how YCL asters interact at common boundaries. We quantify their position and variable number in the transgenic embryos, where YCL asters group in one or more spherical latitudes. This variability thus encodes different configurations, compatible with development, highlighting the yolk domain as a plastic but robust region. We also manage to induce the formation of YCL asters in wild type embryos upon the transient expression of the MT associated proteins DCLK (doublecourtin-like kinase) or DCX (doublecourtin), important for MT stabilization and nucleation (Moores *et al.*, 2006; Ramkumar, Jong and Ori-McKenney, 2018). We address how the presence and number of YCL asters impact on epiboly progression.

As LSFM is well suited to assess the yolk MT organization in the embryo as a whole, we manage to link different MTOCS in time and in space and to study the overall distribution of MTOCs in the yolk sphere. The large syncytial yolk cell (~700-800µm) is similar in size to amphibian zygotes (~1200µm) and far exceeding the size of standard somatic cells. Therefore, it is an ideal model for studying MT based spatial organization in big cells. We propose that the mechanism (i.e the formation of multiple MT asters) shown here could exemplify a special adaptation of conserved mechanisms. In addition, it allows to underscore unnoticed capabilities of the yolk cell.

Finally, we also identify the key molecules of MTOCs in the zebrafish yolk cell. Amongst them, we determine that centrin highlights both centrosomal and non-centrosomal MTOCs in the yolk cell and allows us to follow the potential reassignment of new sites as MTOCs over time.

RESULTS

The yolk MT network organizes into different microtubule organizing centers (MTOCs) during early zebrafish development

Thanks to our custom-made high throughput multi-view light sheet imaging approach, we have access, with high temporal and spatial resolution, to the whole embryonic sphere throughout zebrafish early developmental stages. LSFM provides high resolution with high signal to noise ratio images in a very efficient way. This allows visualizing even the internal structures of the yolk sphere, with less photo-bleaching and photo-toxicity (Olarte et al., 2018; Andilla et al., 2017). Additionally, our original high-throughput sample mounting solution based on fluidic sample loading (Gualda et al., 2015) permitted the study of a large population (over one hundred) of embryos preserving sample viability and in a highly reproducible way. This has allowed us to show the great phenotypic variability on the yolk MT network. Some examples are displayed in Figure 1.

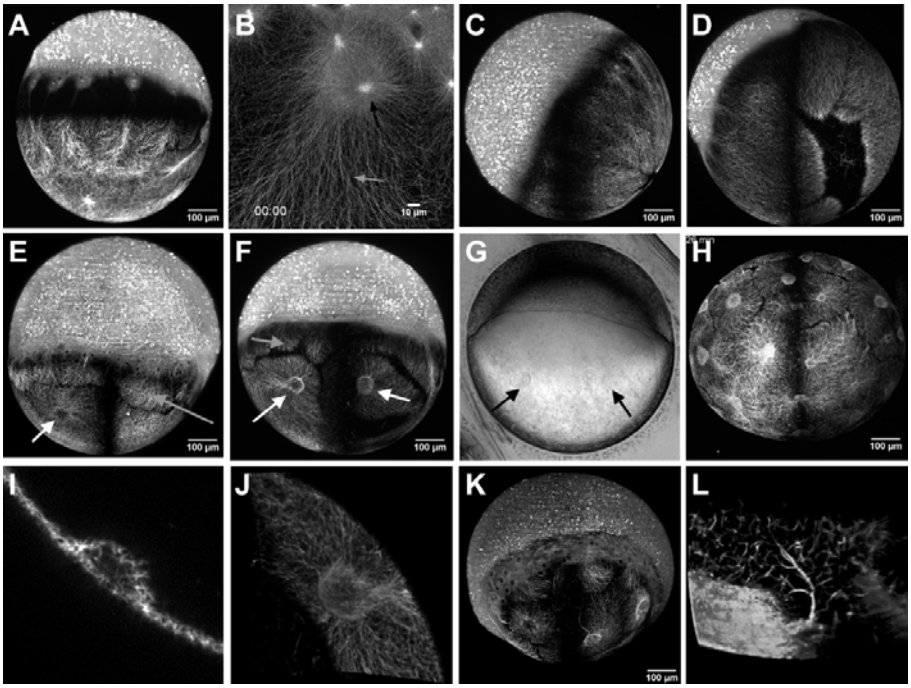

Figure 1. Variability on yolk microtubule organization centers (MTOCs) in dclk2-GFP transgenic zebrafish embryos using light sheet fluorescence microscopy. **(A)** At sphere stage, parallel MT arrays emerge from YSL, covering the YCL. At the animal pole, mitotic spindles of dividing cells are also visible. **(B)** LSCM zoom into the YSL, we can see meshed interconnected MT with apparent spindles during mitosis of e-YSN (black arrow) and the AV parallel YCL MT arrays, emanating from MTOCs associated to the most vegetal e-YSN (grey arrow). **(C)** At 50 % epiboly, the blastoderm occupies half of the embryo sphere. **(D)** Embryo showing defined MT domains and aperture of the vegetal pole. **(E)** Many embryos present YCL asters, a radial MT organization in defined regions (white arrows). A cross section of each YCL aster **(I)** shows an invagination of the yolk membrane, covered with MT. **(F)** These YCL asters organize MT in clear domains, different from the MT network emerging from the YSL (grey arrows). A volume render **(J)** helps highlighting the 3D nature of these structures, also visible in **(G)** bright-field imaging (black arrows). **(H)** Some embryos show up to 22 YCL asters, covering the

entire YCL. In many asters, thicker MT bundles are visible in specific directions. **(K)** Most of the embryos showing YCL asters lack a vegetal pole aperture. In some cases, an aster occupies this position, and occasionally there is a connection to thick MT bundles from the inner MT network **(L)**. All the described features can be clearly observed in the 3D volume rendering in Video S1.

We have primarily used Tg(Xla.Eef1a1:dclk2a-GFP) (from now on abbreviated dclk2-GFP) embryos, as a MT reporter transgenic line. Through the dclk2-GFP line we can observe, before epiboly starts, the presence of the two types of yolk MTs organization already described in the 90's (Solnica-Krezel and Driever, 1994; Jesuthasan and Strähle, 1997). Those are, firstly, meshed interconnected MTs covering the entire YSL corona, with apparent spindles during mitosis of YSN (Figure 1B). Secondly, the animal-vegetal (AV) parallel arrays of MTs of the YCL, emanating from potential MTOCs associated to the most vegetal e-YSN and ending at different latitudes of the yolk cell (Figures 1A and 1B) (Jesuthasan and Strähle, 1997; Eckerle *et al.*, 2018).

At 50% epiboly, when the deep cells engage in the gastrulation movements of involution and convergence, the blastoderm covers almost completely the YSN and their associated MT arrays (Figure 1C). From this point, the possibility to inspect many embryos with our LSFM microscope revealed, despite the classical view, a large phenotypic variability in the MT organization along the yolk cell. While some embryos show clearly the AV parallel arrays, in others these arrays are grouped in fewer well-defined domains. Moreover, some embryos show an opening on the vegetal pole (Figure 1D), while others do not. Finally, and common to most of the analyzed embryos, the vegetal array of MTs organizes in clear and visible compartments that we will call yolk cytoplasmic layer asters (YCL asters*)* (Figures 1E, 1F, 1H and 1K), with MTs radially orienting from each of the domains center. To the best of our knowledge, this is the first time that those structures are reported. Interestingly, a simple observation with bright-field microscopy also reveals invaginations of the yolk membrane at the sites of each YCL aster (Figure 1G). The number of the YCL asters can vary from 0 up to 22 in a single embryo (Figure 1H). A cross-section (Figure 1I) reveals that those YCL asters present a double MT network, one at the yolk surface and another surrounding basally a region with less MT density. A 3D render (Figure 1J and Video S1) shows how those structures resemble a half sphere shape. Remarkably, in some cases, thicker MT bundles from deep inside the yolk mass assemble and extend from the bottom of the asters in a process of MT recruitment (Figures 1K, 1L and S1).

Interestingly, in eggs with many YCL asters, visual inspection suggests that their distribution is not random but occurs in one or more concentric rings around the animal-vegetal axis. To confirm this observation, we calculated the spherical coordinates of the YCL asters. Results are displayed in Figure 2, where we show two representative embryos with four rings (Figure 2 A-D) and a single ring (Figure 2 E-H), respectively. The computation of their polar angles (latitude coordinates, θ) confirms that different asters indeed group in the same latitude (Figures 2B, 2C, 2F and 2G). In embryos with more than one concentric ring, different latitudes can be observed (Figure 2B and 2C). The number of rings in the different embryos is variable, as for the number of YCL asters in a ring (Figures 2I and 2J). Finally, the computation of the aster's azimuthal angles (longitude coordinates, ϕ) (Figures 2D and 2H) showed that asters within a ring are equidistant in a range between 37.5% to 100%, independently of the total number of asters in the ring (Figure 2K). The yolk view was not

always complete due to the embryo position, therefore not all YCL asters were visible. This fact could account for the non-equidistancy portion. In those cases (see asteriks in figure 2D) the distances are doubled since most probably an aster in between was not imaged.

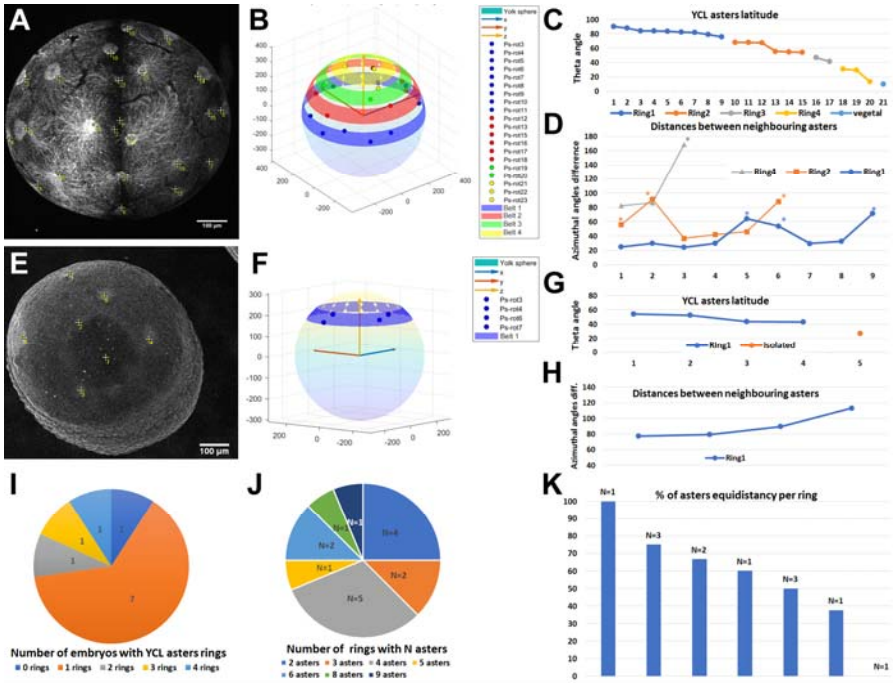

Figure 2. Analysis of the spatial YCL aster distribution in rings. **(A)** Maximum projection of a dclk2-GFP embryo where 22 YCL asters can be identified (yellow crosses) distributed in four rings. **(B)** Projection of the aster position in a sphere. Asters belonging to the same ring are represented by dots of the same color, rings are highlighted as belts at the calculated latitude. **(C)** YCL asters latitude (polar angle). YCL asters are not randomly located but group in four different latitudes (rings) (blue, orange, grey and yellow) and a single aster is found at vegetal pole. **(D)** Azimuthal angles difference between neighboring asters in rings 1 (blue), 2 (orange) and 4 (grey). Asters in this embryo are equidistant in 11/18 cases. For cases they are not (asterisk), we suspect an aster in between could not be imaged. **(E-H)** Same analysis for an embryo with only one YCL asters ring. Here 5 YCL asters can be identified. For this particular case, asters are equidistant: 80, 80, 90 and 110 (5 asters distributed around 360 degrees). **(I)** Plot of the distribution of YCL asters in 0, 1, 2, 3 or 4 rings. The analysis was performed in 11 embryos. **(J)** Quantification of the number of asters in different rings. The analysis was performed in 16 rings. **(K)** Quantification of the equidistance between YCL asters, analyzed in 12 rings. Regardless the total YCL aster number per ring, equidistance ranged between 37.5% to 100%. Only in one case no equidistance was observed. N, number of rings.

209 **YCL asters are transient 3D patterns of radially oriented MTs**

210 To gain insight on the dynamics and the architecture of YCL asters, we next examined them
211 with high temporal and spatial resolution. We could split the temporal YCL asters evolution
212 in four steps: compartmentalization of yolk MTs into distinguishable domains; formation of
213 asters with MTs radially orienting from the center of each compartment; growth of asters;
214 and finally, asters reabsorption below the approaching blastoderm.

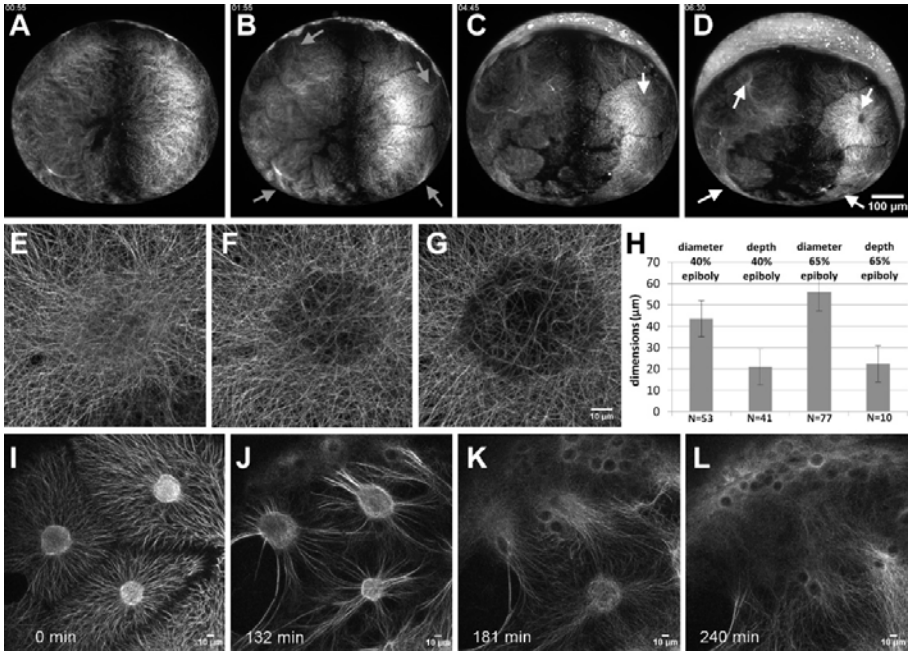

215

216 **Figure 3. The YCL asters form and evolve throughout epiboly.** (**A**) After the last YSN division, the MT network acquires a
217 new configuration. **(B)** At sphere stage, the MT network has rearranged into clear domains, with a central high dense MT
218 bundle emanating from the YSL MTOCs (grey arrow). **(C)** Emerging from those bundles, defined MTs domains start
219 migrating vegetally following a flat to hemisphere transition, leading to the formation of a visible YCL aster (white arrow)
220 with radially oriented MT fibers in the middle of each domain **(D)**. **(E-G)** High-resolution visualization of an aster growth
221 through LSCM. **(H)** After inspection of more than hundred asters in different embryos we observe that, once formed, the
222 depth of the asters keeps constant while their diameter increases. **(I)** The aster domains remain individualized, with clear
223 opposing MT tips. In some cases, the YCL aster core shows a brighter fluorescence signal, while others appear emptier **(G)**.
224 When the marginal blastoderm approaches the YCL asters, the MT network rearranges once again. Thicker bundles are
225 formed and reorient in the AV direction **(J)** and the cores of the YCL asters actively migrate animalwards **(K)** until they
226 disappear underneath the YSL **(L)**. See also Videos S2 and S6.

227 The re-organization of the yolk MT network that gives rise to this scenario begins when the
228 YSN become post-mitotic, that is, when epiboly starts. We clearly observe a transition
229 between a uniformly yolk coverage of MTs (Figure 3A) to the formation of domains (Figure
230 3B), that look independent from each other at this scale of observation. At this point,
231 emerging from the blastoderm, YCL asters form as they migrate vegetally along the MT
232 bundles anchored at the YSL (Figure 3C). At 65% epiboly, just after the formation of the
233 embryonic shield (Warga and Kimmel, 1990; Montero *et al.*, 2005), the e-YSN re-emerge
234 from below the blastoderm and start moving towards the vegetal pole. At this moment, all
235 the previously formed vegetal MTs compartments generate a clearly distinguishable round
236 central region with MT bundles that are radially oriented from it (Figure 3D). YCL asters
237 span the yolk surface and resemble large MTOCs. The degree of epiboly when they form can
238 vary between embryos and, in some cases, the e-YSN mitotic asters coexist with these newly

formed YCL asters (Video S2). In rare cases, we observe the formation of a dynamic vortex-like organization of the yolk MTs prior to the formation of the YCL asters (Video S3), very similarly to *in vitro* reconstitution models (Juniper *et al.*, 2018).

In Figures 3E-G and Video S4 we show, using high resolution LSCM, the initial steps of YCL aster formation. Before an actual YCL aster is formed, a dense central circle of disorganized MTs can be identified (Figure 3E). Later on, the density of MTs is slowly reduced in this central region evidenced by showing a reduced signal (Figure 3F). Progressively a membrane depression forms the final YCL aster (Figure 3G). At this point the surrounding dense network of MTs orients radially from the center of the aster and clear MT domains can be distinguished.

A 3D analysis shows that they change over time from a flat shape to a half sphere shape that is fully filled with thicker MTs bundles. We performed a statistical analysis of the diameter, depth and distribution of more than 80 YCL asters from different embryos. On average, the hemispheres display a maximum diameter of 43 µm at 40% epiboly and 56 µm at 65% epiboly, with a constant average depth of 21-22µm from the base to the vertex (Figure 3H). Zooming into the interaction area between asters, we observe clear boundaries between YCL asters domains (Figure 3I) where MTs seem to repel each other.

Once formed, the YCL asters persist on a quasi-static state and in the same position at the mesoscopic level of observation. Only when the blastoderm undergoing epiboly approaches, YCL asters dynamically move beneath the blastoderm changing their shape (Figures 3I-L and Video S5). We can observe a general displacement of the YCL aster towards the animal pole and a reorganization of the MTs in the aster, from a more uniform distribution to a biased preferred distribution (parallel to the AV direction of epiboly movement) (Figures 3I, 3J and S2). Soon after, the asters interact with the migrating e-YSN at the same time they are reabsorbed beneath the blastoderm (Figures 3K, 3L and Video S6).

As described above, in embryos with many asters we have noticed that the asters organize uniformly forming rings on the YCL at specific latitudes. In those, we observed the synchronous reabsorption of the asters belonging to the same ring. Rings of asters laying towards the more vegetal pole are sequentially reabsorbed, triggered by the proximity of the YSL and blastoderm undergoing epiboly.

MT polymerization and nucleation occur at YSN centrosomes and YCL asters

The above observations suggest that YCL asters could be acting as MTOCs. MTOCs are specific sites where MTs are nucleated and from where filaments grow through polymerization of α- and β-tubulin dimers (Lüders and Stearns, 2007; Wu and Akhmanova, 2017). Probably, the most well-known MTOC is the centrosome used by cells during mitosis. However, in many non-dividing cells, the organization of the MTs is imparted by non-centrosomal MTOCs (nc-MTOCs), whose composition is rather unknown (Muroyama and Lechler, 2017; Sanchez and Feldman, 2017). Nc-MTOCs are thought to contain a shorter list of proteins compared to centrosomal MTOCS, amongst which, there have to be MTs minus- and plus-end-interacting proteins recruited for growing MTs tips (Sánchez-Huertas and Lüders, 2015; Paz and Lüders, 2018). Therefore, to give yolk asters a molecular identity as MTOCs, we analysed the expression of three different proteins (EB3, [illegible]-tubulin and ß-tubulin).

Eb3-mCherry mRNA was injected at one-cell stage dclk2-GFP embryos to label MT plus-ends (Stepanova *et al.*, 2003). Its recruitment into growing MT tips was used as an indicator of the polymerization process during plus-end growth occurring at the yolk MTOCs. Thus, e-YSN centrosomes were marked by EB3 comets as newly polymerized plus ends that emanate from them (Fei *et al.*, 2019) and extended further down along growing MTs (Figures 4A and 4D). EB3 localized to e-YSN centrosomes and the mitotic spindle throughout mitosis, as shown in Video S7. Interestingly, EB3 comets also spread towards the vegetal pole throughout the yolk cell and far from YSN centrosomes (Figures 4B, 4C, 4E and 4F) which could indicate the non-centrosomal origin of some MTs.

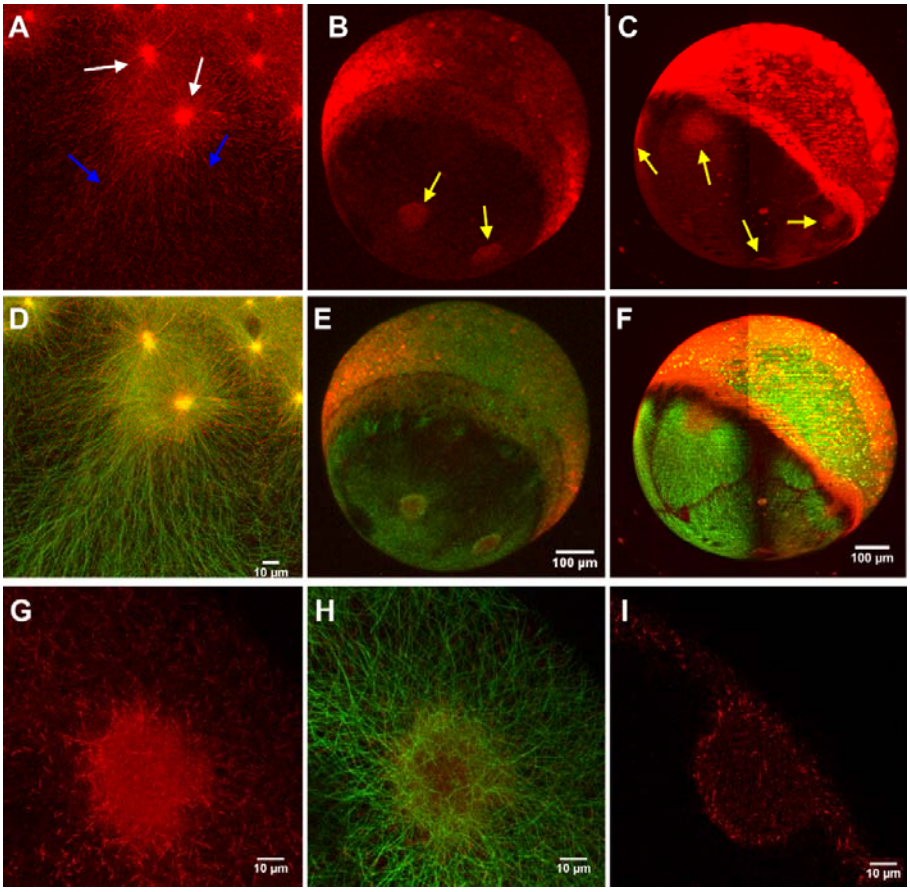

Figure 4. MT polymerization occurs at YSN centrosomes and YCL asters. *EB3-mCherry* injected dclk2-GFP embryos allows us to simultaneously visualize MTs (green) and MTs plus ends (red). EB3-mCherry signal was found: **(A)** in high concentration around e-YSN centrosomes (white arrows), as vegetalward oriented tracks in the YSL (blue arrows) and scattered puncta all along the entire yolk cell. See also Video S7. Whole imaging of the embryos using **(B)** LSCM and **(C)** LSFM also reveals an increase of signal at YCL asters at later stages (yellow arrows). **(D-F)** Merge of the EB3-mCherry and dclk2-GFP signals. **(G-H)** High resolution imaging and **(I)** cross section of a YCL aster shows the MT polymerizing activity at those MTOCs.

In the case of the YCL asters, a high density of EB3-mCherry signal was found at the core of every aster (Figures 4B, 4C, 4E and 4F), suggesting an increase of MT polymerization activity. Zoom into those asters (Figures 4G and 4H) provides a picture of the distribution of EB3 puncta along MTs, with higher signals at the YCL aster core. The cross-section of each of these centers reveals that EB3 distributes mainly in two opposed thin layers separated by a space with lower density of EB3 signal (Figure 4I), very similarly to the MT arrangement as shown in Figure 1I.

γ-tubulin is a MT end protein identified as one of the key nucleator components of MTOCs (Wiese and Zheng, 2006). Although also found in nc-MTOCs, its function there as MTs nucleator, capper or stabilizer is not yet clear (Teixidó-Travesa, Roig and Lüders, 2012; Sanchez and Feldman, 2017). An immunostaining against γ-tubulin protein (Figures 5A-C) allows confirming that both blastoderm (Figure 5B) and e-YSN centrosomes (Figure 5C) contain γ-tubulin. At later stages, when YCL asters are formed, the injection of γ-*tubulin-TdTomato* mRNA at one-cell stage dclk2-GFP embryos (Figures 5D-F) reveals high level of γ-

tubulin protein at the core of every YCL aster, suggesting that yolk asters have a nc-MTOCs identity.

An immunostaining against ß-tubulin highlights MTs and MTOCs, revealing high concentration of ß-tubulin in the YCL asters, a sign of tubulin polymerization on those sites (Figures 5G-H). ß-tubulin fills in the YCL aster volume, in a 2-layered distribution (Figure 5I), similarly to dclk and EB3 proteins (Figures 1I and 4I, respectively).

In conclusion, the localization of EB3, γ-tubulin and ß-tubulin indicates that not only e-YSN centrosomes, but also YCL asters are sites of MT nucleation and growth.

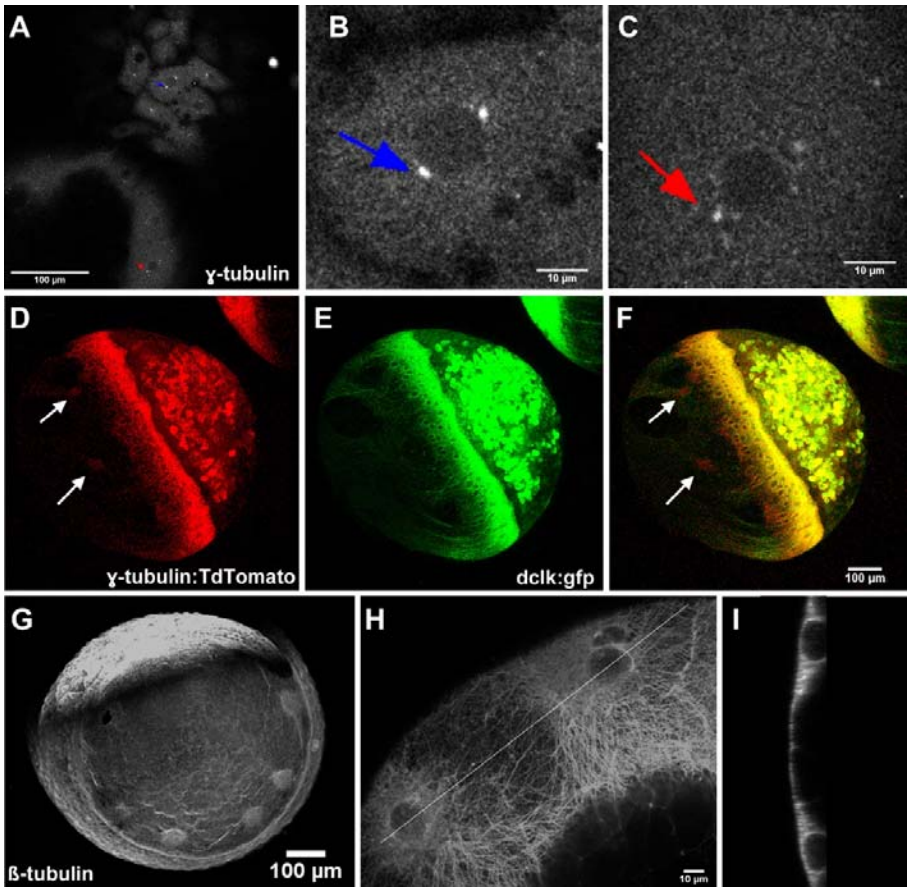

Figure 5. MT nucleation occurs at YSN centrosomes and YCL asters. -tubulin expression can be observed through **(A-C)** immunostaining on fixed embryos and **(D-F)** *-tubulin-TdTomato* mRNA, coinjected with *dclk2-gfp* mRNA. Signal has been found in **(B)** blastoderm centrosomes (blue arrow), **(C)** e-YSN centrosomes (red arrow) and **(D and F)** YCL asters (white arrows). **(G)** ß-tubulin protein is detected in MTs and in high density in YCL asters **(H)**. **(I)** Re-slice of two neighboring YCL asters shows that ß-tubulin fills each aster 3D volume. Images obtained through LSCM.

341 **Centrin highlights centrosomal and noncentrosomal MTOCs in the yolk cell**

342 To further characterize the molecular nature of the different yolk MTOCs we transiently
343 expressed a centrin-GFP construct by injection of the corresponding mRNA into wild type
344 embryos at one cell stage. We observe a diffuse signal in the nucleus and the cytoplasm of
345 the blastoderm cells and the YSL, as well as brighter concentrations on both cells and e-YSN
346 centrioles and other particles around the yolk membrane. This allowed to directly visualize,
347 for the first time to our knowledge on zebrafish embryos, the centrosomic centrin that
348 organizes the YSN mitotic spindles (from now on referred to as *Centrosomal Centrin*, CC)
349 (Figures 6A and 6C). We found out that the same structures also contain ?-tubulin,
350 highlighted with an antibody against the endogenous protein (Figures 5A-C, 6B and 6C).
351 Interestingly, we discovered an independent second set of centrin within the YSL not
352 associated to YSN (from now on *Anchoring Centrin*, AC), to anchor the AV parallel MT arrays
353 (Figure 6D). Finally, a third set of centrin (from now on *Flowing Centrin*, FC), dispersed along
354 the yolk cytoplasm, flows towards the animal pole along the MT network towards the YSL
355 (Figure 6E). This retrograde flow takes place from blastula stages and continues even after
356 YSN have become post-mitotic (Video S8). In few embryos, we also found a higher
357 concentration of centrin signal all over the hemisphere with some distinguishable, highly
358 dynamic, dense centers (Figure 6F). Remarkably, these centers resemble, in terms of size,
359 morphology and dynamics (Video S9), the YCL asters observed in the Tg dclk2-GFP embryos.
360 Although unusual, it is sometimes possible to find asters in wt embryos. This suggests that
361 YCL asters may also contain an aggregation of centrin molecules. We tried, unsuccessfully,
362 to develop a red version centrin tag in order to verify our observations on dclk2-GFP
363 embryos. In any case, the identification of these four different subsets of centrin protein
364 (CC, AC, FC and within the YCL asters) reveals the high complexity of the yolk MT
365 organization.

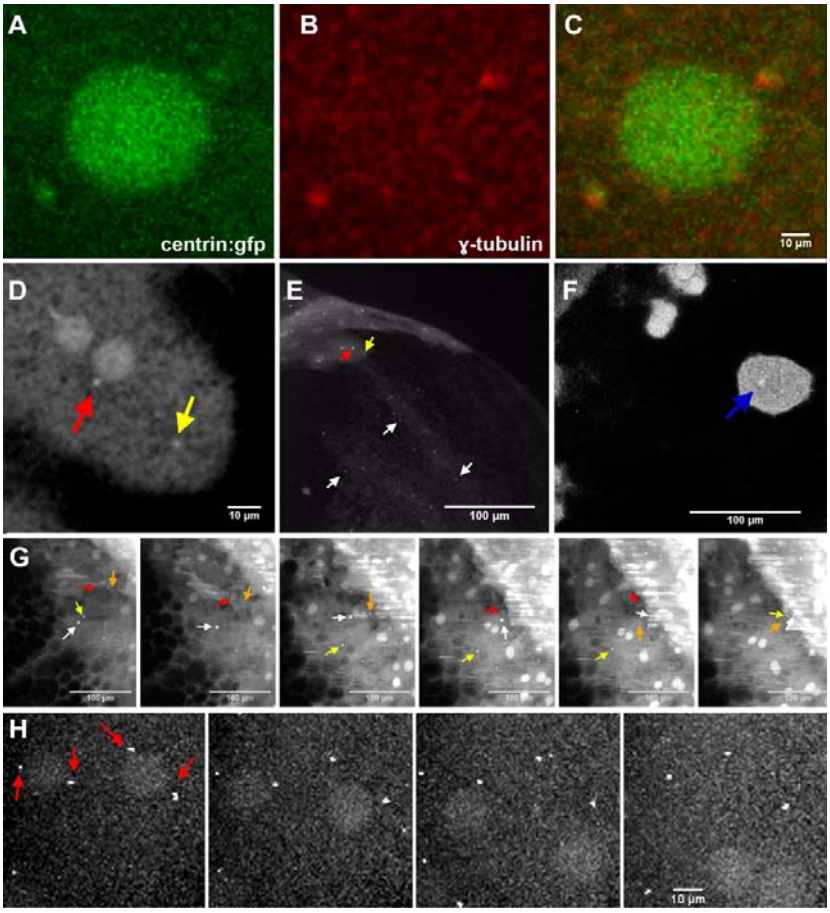

Figure 6. Centrin highlights centrosomal and non-centrosomal MTOCs in the yolk cell. (A) Centrin-GFP is expressed in e-YSN centrosomes and as a diffuse signal in e-YSN nuclei. **(B)** In comparison, γ-tubulin is only found at e-YSN centrosomes. **(C)** Merge of centrin and γ-tubulin signals. High centrin concentration can also be found at: **(D)** the YSL but not associated to YSN (*Anchoring Centrin*, AC), from where the AV MT arrays emerge (yellow arrows); **(E)** the yolk membrane, distributed as scattered puncta (white arrows), that flow animalwards, following MT arrays (*Flowing Centrin*, FC); and **(F)** the core of structures similar to the described YCL asters (blue arrow), visualized with LSCM. Also see Video S9, where centrin accumulation in the YCL resembles by shape, dimensions and dynamics, dclk2-GFP asters. **(G)** Here, zoom into the YSL region, where the interaction between FC (white arrow), AC (yellow arrows) and CC (red and orange arrows) suggests MTOCs functional reassignment by centrin re-localization during epiboly. Video S10 shows FC moving animalwards and its interaction with AC and CC, while epiboly progresses. Tiles in **(G)** are snapshots of a time lapse. **(H)** High resolution LSCM visualization of the YSN migration process initiation. The e-YSN are visible by a centrin diffuse signal and start migrating when centrosomes (red arrows) dettach. Tiles in **(H)** are snapshots of a time lapse.

The simultaneous visualization of all those different components through LSFM, allows us to describe a systemic centrin behaviour along the whole embryo, and specially the yolk cell, during all the epiboly process. As blastoderm and YSN divide, centrioles and nuclei are clearly visible allowing the tracking of mitotic processes. Interestingly, e-YSN centrioles remain after e-YSN exit the cell cycle. Afterwards, when e-YSN stop dividing, many bright FC puncta migrate from the vegetal pole towards the YSL following determined pathways, most likely streams of highly concentrated yolk MTs. These vesicles show a dynamic behaviour, with a tendency to aggregation. Surprisingly, we observed how those vesicles scan the YCL and interact with the e-YSN centrioles (Figures 6G and Video S10). We could clearly observe that at a specific moment, centrioles seem to jump out/detach of the YSL membrane. After the release of the centrioles, e-YSN start a fast migration towards the vegetal pole of the

embryo (Figure 6H). Travelling FC puncta as well as CC migrate underneath the blastoderm as e-YSN migrate vegetalwards. As epiboly progresses and once e-YSN dissociate from their centrioles, the latter seem to be free to move within the YSL and/or actively pulled away by forces applied by the YSL cytoskeleton. In some cases, e-YSN centrioles seem to be dragged together with the traveling FC puncta and “disappear” beneath the blastoderm, within the internal-YSL (i-YSL), where we suspect they also undertake a role to organize the i-YSL MT network.

401 **The yolk MT network adopts different configurations in relation to the expressed levels of**
402 **MT nucleating proteins (DCLK and DCX)**

403 Next we sought to understand the mechanism responsible for the variability observed in
404 dclk2-GFP embryos yolk MT organization. We combined data from our high-throughput
405 LSFM microscope with brightfield inspection in order to screen tens of Dclk2-GFP transgenic
406 embryos. We confirmed that the number of YCL asters amongst eggs laid by different
407 females differ in number, although it is on average repeated across different layings of given
408 females. We have identified at least 8 females with offspring displaying this particular
409 phenotype, and calculated the average number of YCL asters that the progeny of a specific
410 female presents. This ranges between 0 and 22, depending on the female under analysis
411 (Figure 7A). The presence of YCL asters in the Dclk2-GFP transgenic line is transmitted across
412 generations and therefore does not prevent development, i.e. eggs develop and become
413 fertile adults.

414 To understand if the different yolk MT phenotypes had an impact on epiboly progression,
415 we monitored epiboly extension of the progeny of different transgenic fish. We found that
416 epiboly is slower in Dclk2-GFP eggs with more YCL asters. While wt embryos (N=10) and
417 embryos (N= 10) with low number of YCL asters were at 50% epiboly (100%), their sibling
418 embryos (N=12) with many YCL asters were still at sphere-doming stage (100%), and this
419 delay persisted throughout epiboly (Figure 7 B).

420 In an aim to find the molecular mechanism behind the different observed yolk MT
421 configurations, and suspecting a correlation with different dclk protein levels, we also
422 performed *dclk-gfp* RNA injections in wt eggs at one cell stage, at different amounts (50 pg,
423 100 pg, and 200 pg). 100pg *dclk-gfp* RNA dose is able to induce the formation of YCL asters,
424 that become bigger at 200pg dose. Already from 100pg dose we observe a delay in epiboly
425 progression: while the wt embryos (N=30) and their 50pg-injected siblings (N=20) are at
426 60% epiboly (100%), the 100pg (N=35) are at 50% epiboly (40%) and 30% epiboly (60%), and
427 200pg-injected siblings (N=20) are at 30% epiboly (100%). Finally, 100pg injected embryos
428 develop a shorter axis at 24hpf and 200pg dose produces body malformations and a
429 complete lack of body axis extension in the most severe cases (Figure 7C).

430 Interestingly, asters can also be produced in the presence of low levels (50pg) of the paralog
431 gene doublecourtin (DCX), by the injection of *DCX-gfp* RNA at one cell-stage. The
432 overexpression produces big asters in the YCL that resemble those obtained in the *dlck-gfp*
433 RNA injected embryos. They also display a dose-dependent delay in epiboly and
434 developmental defects apparent at 24hpf (Figure 7D).

435 In conclusion, these experiments show that increasing the levels of these two closely related
436 members of MT nucleating proteins family creates new scenarios. We observe that the yolk
437 MT network, normally uniformly covering the yolk cell can re-organize into a multi-aster MT
438 network. As long as the protein levels are kept in an appropriate range (stable transgenic
439 line or low dose injection of corresponding construct) the phenotype is compatible with
440 development, at this spatio-temporal window of observation. This represents an example of
441 plasticity but robustness in development and indicates that this domain has the potential,
442 both molecularly and biophysically, to change and adapt.

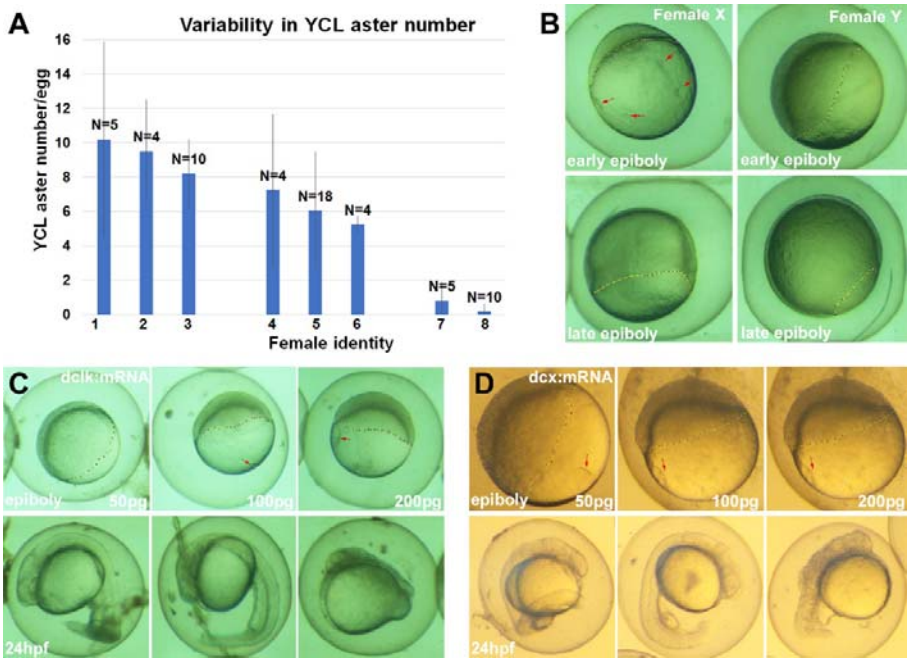

Figure 7. Natural and induced variability in YCL aster features and their impact on early development. (A) Comparison between the average number of YCL asters in eggs of selected Tg dclk2-GFP females: ≥8 YCL asters (females 1-3), between 3 and 7 YCL asters (females 4-6) ,≤2 YCL asters (females 7-8). N stands for the total number of eggs analyzed for the different females. **(B)** Brightfield imaging on representative sibling embryos from different Tg dclk2-GFP females: female X, medium number of asters, (10 eggs analyzed) and female Y, low number of asters, (10 eggs analyzed) at early (upper row) and late (bottom row) epiboly stages (epiboly extension: dashed yellow line. YCL asters: red arrows) **(C)** *dclk2-gfp* mRNA injections partially recapitulate the transgenic phenotype. Upper row: increasing mRNA doses proportionally induce a delay in epiboly (dashed red line) (Wt embryos, N=30; 50pg-injected embryos, N=20; 100pg-injected embryos, N=35; 200pg-injected embryos, N=20). Ectopic asters (red arrows) are formed from 100pg dose. Lower row: development follow up. **(D)** Equivalent experiment with *DCX-gfp* mRNA injections produces bigger asters (upper row, red arrows) and developmental defects (lower row) at lower doses compared to experiment in **(C).**

462

463 DISCUSSION

464 A MT is a self-organization system in which tubulin monomers organize into dynamic
465 filaments. A next level of complexity, i.e. the generation of a 3D pattern such as an aster,
466 involves nucleation, filament dynamics and molecular motors (Nédélec, Surrey and Karsenti,
467 2003). *In vitro* reconstitution experiments show the formation of individual asters in
468 polymer-stabilised microfluidic droplets, by the molecular motor-mediated contraction of a
469 spherical network (Juniper *et al.*, 2018). *In vivo*, a radial rearrangement of MTs in fish
470 melanophore fragments is achieved through dynein-dependent MT nucleation (Vorobjev,
471 Malikov and Rodionov, 2001). The aster-type pattern allows to explore the intracellular
472 space and to define the position of the organelles through interaction with MT motor
473 proteins. In this work, we discover MT asters in the zebrafish YCL and thus we update the
474 current knowledge of zebrafish yolk MT organization. Despite the fact that it has been
475 shown that yolk AV parallel MTs arrays are essential for the epiboly of the e-YSN (Solnica-
476 Krezel and Driever, 1994; Fei *et al.*, 2019), it turns out to be difficult to assess specifically the
477 function of YCL asters. Further YCL asters interference experiments by locally applying
478 nocodazole in the yolk or by uncaging a photoactivatable derivative of the MT
479 depolymerising drug combretastatin (Wühr et al., 2010; Costache et al., 2017) could
480 contribute to explain YCL asters role. Preliminary efforts trying to confine the drug effect in
481 the YCL asters are being conducted. We hypothesise that they are used for mechanical and
482 structural support of the huge zebrafish yolk cell during epiboly, and that they form via a
483 combination of MT nucleation and molecular motors confined in the spherical embryo. The
484 profound plasma membrane deformations identified with bright field microscopy (Figure
485 1G) indicate potential MTs anchoring sites, providing enough mechanical force to induce
486 those deformations. In these sites, YCL asters would be serving for mechanical support.
487 Indeed, it is known that cytoskeletal elements can pull membranes by polymerization or
488 with the help of motor proteins (Solinet *et al.*, 2013; Jarsch, Daste and Gallop, 2016).

489 Comparing to previous literature, the new array of yolk MTs that we describe in this work is
490 different from the AV oriented YCL longitudinal MTs that e-YSN use to migrate vegetalwards
491 (Solnica-Krezel and Driever, 1994; Fei *et al.*, 2019). In many embryos there is a clear MT void
492 space between the AV MT arrays emerging from the blastoderm and the domains formed by
493 the YCL asters. In fact, we found that e-YSN migration along the YCL longitudinal MTs occurs
494 concomitantly with the presence of these vegetal YCL asters (Figures 3K and 3L and Video
495 S5). In any case, until the MT network is re stablished, during YCL aster reabsorption, e-YSN
496 migration seems to be paused, confirming the need of the AV MT network in order to move
497 forward.

498 Despite the work done with the reconstitution of multiple large asters in a cell-free system
499 (Mitchison *et al.*, 2012; Ishihara *et al.*, 2014; Ishihara, Korolev and Mitchison, 2016), to our
500 knowledge there is no report of live non-artificial models forming big multiple MTOCs in an
501 individual cell, with the exception of the transient formation of several small MTOCs in the
502 immature mouse oocyte (Schuh and Ellenberg, 2007; Li and Albertini, 2013). Our data
503 supports that multiple YCL asters form naturally in many of the analyzed eggs, and therefore
504 the zebrafish yolk cell arises as a promising natural model where to analyze aster-aster

interaction zones (Figure 3I). In our model, these regions are very similar to the boundary zones between non-sister asters following polyspermic fertilization in amphibian embryos. Most probably, YCL aster growth is limited by the presence of the neighboring aster, where anti-parallel MTs overlap (Mitchison *et al.*, 2012). In fact, previous extensive studies have reported that Aurora B kinase is key for the formation of asters boundaries in *Xenopus* extracts and between asters in the midplane of cleaving *Xenopus* zygotes (Field, Pelletier and Mitchison, 2019). How similar our boundary zones are to other studied boundaries, both biophysically and molecularly, remains to be examined.

Moreover, we observe an almost perfect synchrony between the multiple YCL asters, equidistant to the YSL, across the different steps leading to their formation and re-absorption, pointing to 1) a global coordination mechanism and to 2) a tight mechanical dependence on the epiboly process. The radial distribution in concentric rings around the AV axis without any apparent dorso-ventral bias, also supports this last idea, since epiboly is essentially a radially symmetrical process in this direction. We found that YCL asters are not randomly located in the embryonic sphere. On the contrary, they tend to group in the same latitude (or various latitudes when more than one ring is formed) and to keep a quasi-constant distance between them (Figure 2). We suggest that this distribution is related to geometrical or mechanical constrains. The YCL asters resemble polygon-like structures that cover the exposed yolk surface (see figure 2A) (it remains to be tested if the non-exposed, i.e underneath the blastoderm, is also covered by YCL asters). Thus, remarkably, the yolk is revealed as a biological model for the uniform distribution of many points in a (hemi)sphere. Accessing the totality of the yolk sphere maybe by mechanical removal of the blastoderm would allow to test if the yolk MT network is a solution in nature for the classical best packing problem in spheres and minimal energy point configurations (Saff and Kuijlaars, 1997; Brauchart and Grabner, 2015).

In this work we prove that e-YSN spindles are organized through MTOCs, by the localization of EB3, γ-tubulin and centrin proteins. Our observations agree on the experiments conducted by (Fei *et al.*, 2019) where e-YSN centrosomes are highlighted with an EB3-tagged construct. We also show that the presence of EB3 and γ-tubulin in YCL asters unequivocally indicates that they are sites of MT nucleation (Figures 4 and 5). Finally, this is supported by the localization of high levels of β-tubulin, used for MTs assembly, in the asters (Figures 5G-I).

In fact, LSCM and LSFM have been instrumental for the localization and dynamics of the different MTOCs components and to understand that several MTOCs need to be in place to organize a network of such dimensions, that dramatically changes over the early stages of zebrafish development. In particular, we prove that transient expression of centrin-GFP protein (CC, AC and FC -see section 4 of Results) successfully highlights centrosomal and noncentrosomal MTOCs in the yolk cell, in agreement with (Paoletti *et al.*, 1996) that stated that more than 90% of centrin is not associated with the centrosome fraction. The YCL FC moves animalwards, towards the YSL, and seems to follow the AV MT parallel arrays tracks (Video S8). Travelling FC puncta briefly interact with CC centrioles (Video S10) and migrate underneath the blastoderm as e-YSN migrate vegetalwards. We suggest that this FC-CC centrin interaction is probably part of the process that actually triggers the e-YSN migration. Interestingly, e-YSN centrioles disassociate from these nuclei, most probably through a

549 detachment mechanism from the nuclear envelope, and become "free" to drift away from
550 the nuclei (Figure 6) (Archambault and Pinson, 2010). From the stage e-YSN exit the cell
551 cycle, we assume that their centrosomes lose their activity as MTOCs, and new cellular sites
552 are specified and activated to acquire this function within the huge yolk cell. In
553 differentiated cells, the loss of centrosomal MTOC activity and the formation of non-
554 centrosomal sites can happen through different mechanisms (Keating *et al.*, 1997; Bartolini
555 and Gundersen, 2006; Brodu *et al.*, 2010; Muroyama and Lechler, 2017; Sanchez and
556 Feldman, 2017) although most studies point to protein localization and pericentriolar
557 material delocalization as the most common ways of regulation. However, in our system we
558 hypothesize that the mechanism is slightly different, because the formation of the novel
559 more vegetal yolk MTOCs does not imply the disappearance of the e-YSN CC (Figure 6).
560 Concomitantly, yolk MT network organization seems to be governed by several MTOCs
561 elsewhere, rather than only the centrosomal-MTOCs (e-YSN CC). This would imply the
562 recruitment of centrin and/or other key molecules to those new sites probably through a
563 MT and motor proteins-dependent mechanism (Dammermann and Merdes, 2002). Centrin
564 behaviour in our model supports this idea: first, we observe that e-YSN CC seems to be
565 recycled, because e-YSN centrioles do not disappear. Second, at middle to late epiboly
566 stages, we observe centrin expression in structures located more vegetally, resembling YCL
567 MTOCs both by location and behavior. Thus, centrin is at the core of both centrosomal and
568 non-centrosomal yolk MTOCs that co-exist in the embryo. The observed centrin temporal
569 and spatial dynamics inform on the biology of centrosomes and points to a complex whole-
570 embryo large-scale regulation that deserves future study.

571 It has been proposed that asters can form in different ways either in natural or artificial
572 conditions (Nédélec, Surrey and Karsenti, 2003). We have specifically investigated the dclk2-
573 GFP transgenic line and found that it represents a scenario in which the phenotypic
574 variability (absence/presence and different number of asters) accessed through LSFM could
575 reflect the different levels of dclk protein expressed in the progeny of different tg dclk2-GFP
576 individuals (Figures 7A and 7B). Importantly, this provides evidence that the yolk MT
577 organization doesn't follow a rigid scheme. We propose that the variability observed is a
578 possible outcome of the use of the Tol2 transgenesis method (Kawakami, 2007), which
579 could have produced different integration sites of the Tol2 element in the respective
580 genomes. This suggests that our model of study is the result of an overexpression
581 phenotype (Prelich, 2012) compatible with normal development as long as the gene is
582 expressed at an appropriate range level. Thus, *dclk2* or *DCX* mRNA injections are not neutral
583 at higher doses (Figures 7C and 7D), while the transgenic line is stable and all analysed
584 phenotypes are compatible with development, probably because expression levels are kept
585 within an appropriate range. We speculate that increasing the levels of DCLK or DCX causes
586 the formation of ectopic nucleation sites, in our case YCL asters, similar to γ-tubulin or
587 RanBPM overexpressions (Shu and Joshi, 1995; Nakamura *et al.*, 1998). However, the
588 transient expression induces the uncontrolled formation of YCL asters that are bigger and
589 misslocalized when compared to the asters formed in the stable transgenic line, giving rise
590 to developmental defects.

591 We rarely found YCL asters in wt "naked" eggs (non-injected, non-transgenic), which could
592 be explained in two ways. On one hand, despite YCL asters might exist, the expression levels
593 of the molecules recruited to those sites are too low to be detected with our tools and to
594 generate big asters capable to induce the profound yolk membrane deformations observed

595 with bright-field imaging (Figure 1G). On the other hand, it is possible that wt embryos
596 organize the yolk MT network in an alternative way and YCL asters are an example of the
597 creation of a functionality that is normally hidden in the system, that is triggered by the
598 overexpression of MT nucleating proteins in a particular time and territory.

599 With this work we have specifically investigated the organization of the yolk MT network
600 during zebrafish epiboly. The transgene-mediated phenotypic variability that we have found
601 points to the yolk domain as a plastic but robust territory, able to present diverse
602 configurations. This variability however encloses universal mechanisms for MT organization,
603 especially in large cells, like the zebrafish yolk cell, where different MTOCs are in place to
604 ensure development. Finally, our results underscore the importance of the observation of
605 the embryo as a whole, allowing to connect events in time and in space.

606

607 METHODS

608

609 ZEBRAFISH STRAINS

610

611 AB and Tg:(XlEef1a1:dclk2a-GFP) strains (from Marina Mione, CIBIO, University of Trento,
612 Italy) (Tran, L.D.,et al., (2012) were used. Animals were housed under standard conditions.

613

614 Zebrafish embryos were kept in E3 medium (**Nüsslein**-Volhard and Dahm, 2002) and staged
615 as previously described (Kimmel and Law, 1985). Embryonic manipulations were done in E3
616 medium. The embryos analyzed in our study are always the result of outcrosses between
617 Tg:(XlEef1a1:dclk2a-GFP) females with AB WT males. Up to 15 Tg:(XlEef1a1:dclk2a-GFP)
618 females of successive generations were used in this work.

619

620 DNA CONSTRUCTS AND mRNA INJECTIONS

621

622 The following expression constructs were used: EB3-mCherry (Stepanova *et al.*, 2003),
623 centrin-GFP, β-tubulin-tdTomato, (kindly provided by Virginie Lecaudey, Goethe-Universität,
624 Frankfurt), dclk2-GFP (kindly provided by Marina Mione, CIBIO, University of Trento) and
625 DCX-GFP (kindly provided by Esteban Hoijman, CRG, Barcelona). mRNAs were synthesized
626 using SP6 mMessage machine kit (Ambion®, Life Technologies, Germany), after NotI
627 linearization. Zebrafish embryos were injected using glass capillary needles (Harvard
628 apparatus 30-0020 GC100F-15) which were pulled with a needle puller (Sutter P-97), and
629 attached to a microinjector system (World Precise Instrument PB820). Unless otherwise
630 indicated, 100 pg of EB3-mcherry mRNA, centrin-gfp mRNA, dclk-gfp mRNA or β-tubulin-
631 tdTomato mRNA were injected into 1-cell stage embryos.

632

633 WHOLE-MOUNT IMMUNOHISTOCHEMISTRY

634

635 Mouse anti-β-tubulin antibody (E7, Developmental Studies Hybridoma Bank, DSHB) was
636 used at 1:200 and mouse anti-γ-tubulin antibody (T5326 Sigma-Aldrich) was used at 8ug/ml.
637 The secondary antibody was in-house conjugated (Bálint *et al.*, 2013) to the Abberior STAR
638 635P fluorophore (Sigma) and used at 8ug/ml.

639

640 γ-tubulin staining was performed as previously described (Li-Villarreal *et al.*, 2015) Briefly,
641 embryos were fixed in 4%PFA overnight at 4ºC. Fixed embryos were washed several times in
642 PBS and dechorionated. Permeabilization was done in 0.3% Triton X-100 (in PBS) for 1 h,
643 exchanging buffer every 15'. Blocking was performed in blocking solution (1% BSA in 0.3%
644 Triton X-100 in PBS) for 2 hours, at RT. Embryos were incubated with γ-tubulin primary
645 antibody in blocking solution overnight at 4ºC. After washing the embryos in 0.3% Triton X-
646 100 in PBS overday, they were incubated in the secondary antibody in blocking solution
647 overnight at 4ºC. After 3-4 washes in PBS, the embryos were ready to be mounted and
648 imaged.
649 ß-tubulin antibody staining was performed as previously described (Topczewski and Solnica-
650 Krezel, 1999) with some modifications. Briefly, embryos were dechorionated and fixed in
651 MT assembly buffer (80 mM KPIPES (pH 6.5), 5 mM EGTA, 1 mM MgCl2, 3.7%formaldehyde,
652 0.25% glutaraldehyde, 0.5 uM taxol, and 0.2% TritonX-100) for 6 hours at RT. Fixed embryos
653 were dehydrated and kept in methanol at –20°C overnight, or for several days. After, they
654 were washed several times in PBS containing 0.1% NP40, for re-hydration. Re-hydrated
655 embryos were then incubated in 100mM NaBH4 in PBS for 6-16 hours at RT, and washed
656 extensively in tris buffered saline (TBS). Blocking was performed in blocking solution (2%
657 BSA in TBS) for 30' at RT. Embryos were incubated with β-tubulin primary antibody in
658 blocking solution overnight at 4ºC. After washing them 4-5 times in TBS, they were
659 incubated in the secondary antibody in blocking solution for 2-3 hours at RT. After 3-4
660 washes in TBS they were ready to be mounted and imaged.
661
662
663
664
665 IMAGING SET UPS AND SAMPLE PREPARATION FOR LIVE AND FIXED IMAGING
666
667 LSCM was performed on a commercial Leica SP8 equipped with a supercontinuum white-
668 light laser (KTT) and Hybrid detectors, and with HC PL APO CS2 10x/0.40 DRY and HC PL APO
669 CS2 63x/1.40 OIL objectives. For live imaging, dechorionated embryos were mounted in
670 0.5% low melting point (LMP) agarose (ref) in E3 medium, on glass bottom dishes (MatTek).
671 Fixed samples were mounted in 1% LMP agarose in PBS, on glass bottom dish (MatTek).
672
673 LSFM imaging was performed using a custom-made light-sheet set up, an improved version
674 of our previous design (ref), called Flexi-SPIM (ref). For illumination we used 488 and 561
675 nm lasers (Cobolt, MDL488 and MLD561) and two air objectives (Nikon 4x, NA0.1). For
676 fluorescence detection we used water dipping objectives (Nikon 10x, NA0.3 and 20x, NA
677 0.5), filters and a sCMOS camera (Hamamatsu OrcaFlash4 v2). Thanks to our configuration,
678 multiple views of the specimen can be visualized, providing in toto embryo representations.
679 We realized, along the experiments, that LSFM imaging of the yolk leads image degradation
680 along the illumination axis. This is due to light refraction on the lipid filled spherical yolk cell,
681 that acts as a lens. Sequential side illumination, although requiring a simple fusion process,
682 increases image quality. However, this leads to a blind central region on the data sets. This
683 effect is neglectable in the blastoderm. Embryos were simply mounted, without removing
684 its chorion, within either a 1.5% LMP agarose cylinder or a 1mm inner diameter FEP tube
685 filled with E3 medium.
686

Bright field images were acquired with a scope or the light-sheet set up and a source of white-light, bulb or led, respectively.

IMAGE ANALYSIS

To evaluate YCL asters sizes, the 3D z-stacks were analysed. YCL MT asters' depth and diameter were measured with FIJI in their max value.

For the quantification of the YCL asters number, we manually counted the number of YCL asters on the Z maximum projection of LSFM and LSCM images. Only the eggs offering a vegetal view (the totality of the YCL asters could be accessed) and eggs offering a lateral view, in which radial symmetry could be assumed, were considered. The females were grouped in 3 classes: females producing eggs with many asters (≥8), females producing eggs with an intermediate number of asters (between 3 and 7) and females producing eggs with a very low number of asters (≤2). The analysis includes 8 females in total.

To estimate the local orientation of the MT bundles in YCL asters (N=9) at different distances from the YSL, we used two Fiji plug-ins: OrientationJ (Püspöki et al., 2016) and Directionality (created by Jean-Yves Tinevez, Institute Pasteur). For OrientationJ we used in particular the functionality OrientationJ Analysis to render a visual representation of the orientation of the MTs in the YCL asters, and the functionality OrientationJ Vector Field to create a vector field map of the selected images. To generate the histograms that show the amount of MT bundles in particular directions the local gradient orientation method of Directionality plugin was used. Background was subtracted and a smooth filter was applied (FIJI) in the original images before the orientation analysis were performed.

To determine YCL MT aster distribution over the yolk, 3D stacks acquired either by LSFM or LSCM were analysed. Images relative to a single time point were used, correspondent to the embryo at 50-65% epiboly, i.e. when the YCL asters are clearly visible. A FIJI home-made macro permits to select and export the 3D coordinates of the centre of the embryo, the vegetal pole, and the asters. Elaborating these 3D coordinates through a MATLAB script, the AV axis orientation and the radius of the modelled yolk sphere are obtained. Based on this, a rigid body transformation of all the points is applied, so that the centre of the embryo is coincident with the coordinate origin, and the AV axis aligned along the "z" axis. Describing the YCL MT aster coordinates by mean of spherical coordinates, the latitude (polar angle relative to the AV axis) and the longitude (azimuthal angle) of each of the MT asters are computed. For each embryo, MT asters having a similar latitude (i.e. a maximum of 20 degrees of difference) were considered to belong to the same ring, concentric to AV axis. For each ring, the differences between longitudes of neighbour MT asters were calculated to examine eventual angular equidistance between them. Equidistance is defined as the angular distances' differences is belonging to a 10 degrees range. A total of 11 embryos with at least 4 YCL MT asters were analysed. For angular equidistance analysis, only rings with more than 2 asters were considered. In cases where equidistance is not found, we suspect an aster in between could not be detected from the image 3D field of view.

ACKNOWLEDGMENTS

This project and MB have received funding from the European Union's Horizon 2020 research and innovation programme under the Marie Sklodowska-Curie grant agreement No 721537 "ImageInLife". EG received funding from MINECO/FEDER Ramon y Cajal program (RYC-2015-1793). Authors also acknowledge financial support from the Spanish Ministry of Economy and Competitiveness through the "Severo Ochoa" program for Centres of Excellence in R&D (SEV-2015-0522), from Fundació Privada Cellex, from Fundació Mir-Puig, and from Generalitat de Catalunya through the CERCA program". We thank Virginie Lecaudey, IZNF Germany, and Darren Gilmour, IMLS Switzerland, for the EB3-mCherry, centrin-GFP and γ-tubulin-TdTomato DNA constructs, Marina Mione, CIBIO, University of Trento, for the dclk2-GFP DNA construct and Esteban Hoijman, CRG Spain, for the DCX-GFP DNA construct. We are grateful to Timothy Mitchison for providing the combretastatin drug for preliminary assays. We thank Verena Ruprecht, CRG Spain, Jordi Andilla, ICFO, Spain, and Pilar Pujol, ICFO, Spain, for helpful discussions. We thank Senda Jiménez, CRG, Spain, all SLN-ICFO members and ICFO Biology lab members for their support.

AUTHOR CONTRIBUTIONS

MM designed the experiments. MM, MB and EG conducted the experiments and analysis. MM and EG wrote the manuscript. MB and PL read and edited the manuscript. MM, and PL conceptualized the study. PL supervised the work.

DECLARATION OF INTERESTS

The authors declare that they have no conflict of interest.

SUPPLEMENTARY INFORMATION

Document S1. Figures S1–S2

Supplementary Figure 1: Inner yolk microtubule network and YCL asters

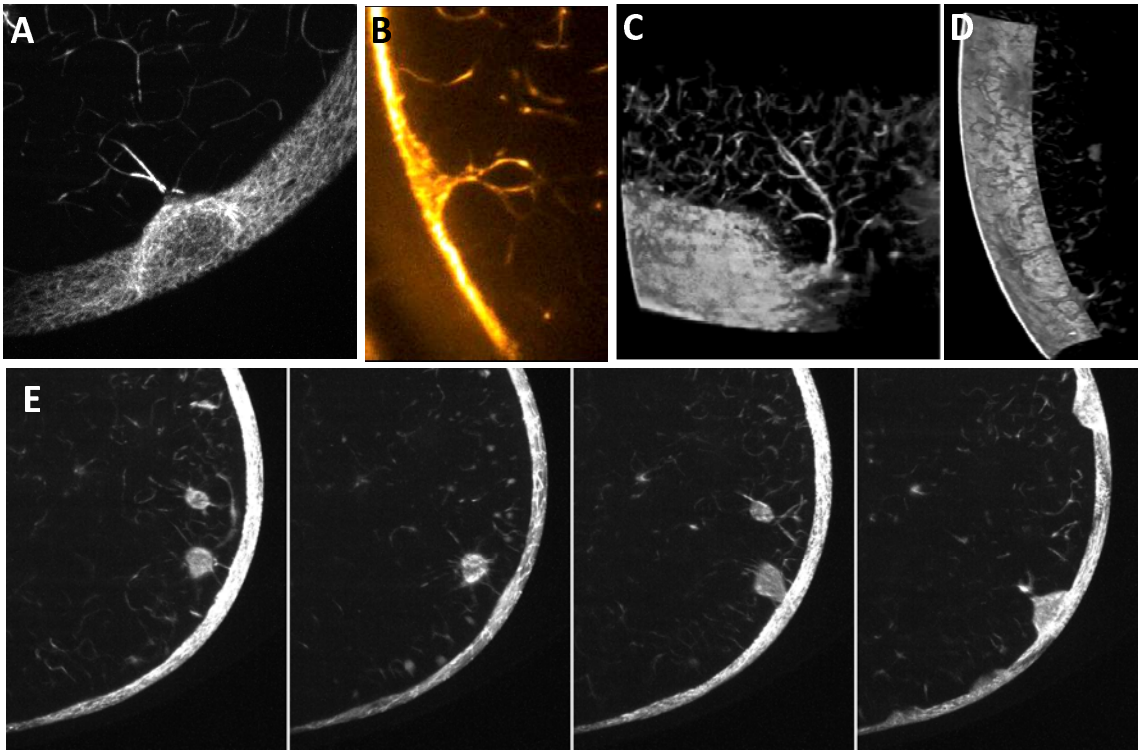

Supplementary Figure 1: Light sheet fluorescence microscopy allows visualizing the inner yolk microtubule network and its interaction with YCL asters. (A-D) In some cases it is possible to observe that YCL asters are able to recruit the inner microtubule network forming dense MT bundles. **(E)** Observing over time a cross section of the embryo it is possible to observe how YCL asters recruit inner yolk MT aggregates. In any case, it is worthy to point out, that those examples do not fully represent the observed dynamics. Normally YCL asters form independently of its interaction with inner microtubules bundles or aggregates.

781 **Supplementary Figure 2: Orientation of the MT bundles within representative YCL asters**

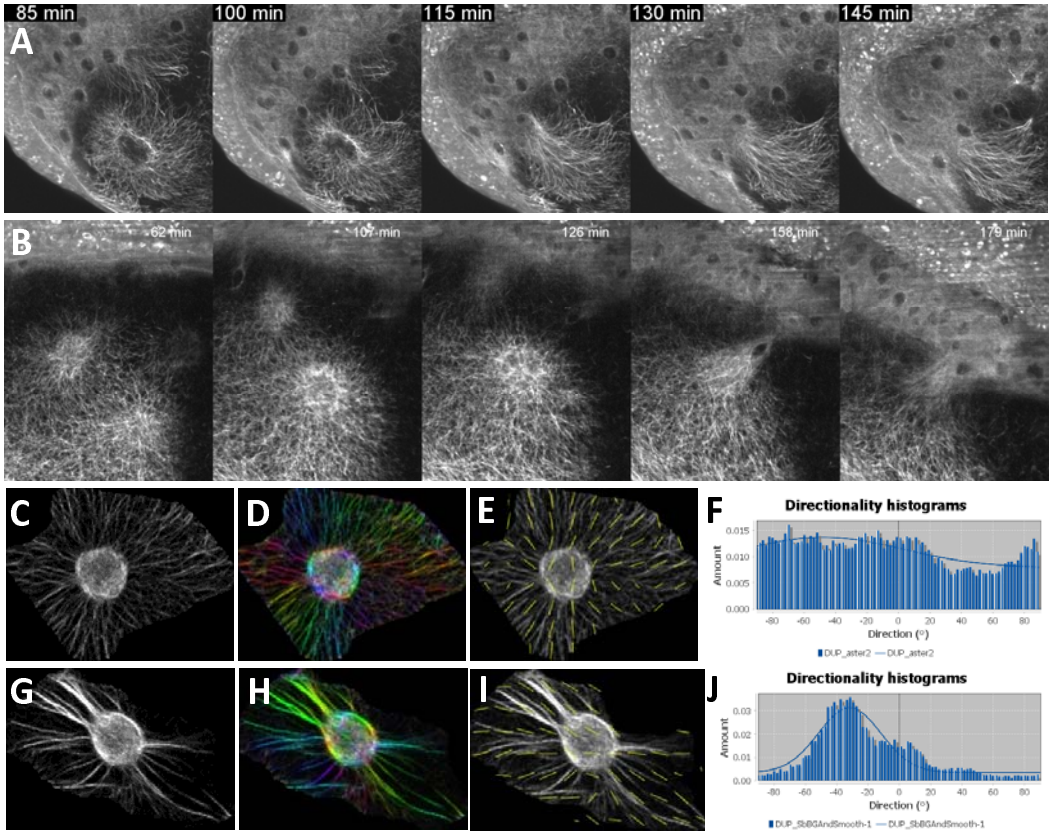

782

783 **Supplementary Figure 2: Orientation of the MT bundles within representative YCL asters regarding distance**
784 **to blastoderm margin. (A)** and **(B)** show two examples of YCL aster reabsorption as the blastoderm margin
785 approaches. To estimate the local orientation of the MT bundles we used two ImageJ plug-in: OrientationJ and
786 Directionality. **(C-F)**: YCL asters not adjacent to blastoderm margin show an isotropic distribution of MT
787 bundles. **(C)** Original image of YCL aster. **(D)** OrientationJ Analysis module performs a visual representation
788 with a color map of the distribution of the MT bundles. **(E)** Vector field overlaid on the original image,
789 performed by OrientationJ Vector Field module. **(F)** Histogram computed with Directionality plugin, indicating
790 the amount of MT bundles in a given direction. This flat histogram indicates a very isotropic MT content in this
791 type of YCL asters. **(G-J)** The same analysis was performed when the blastoderm margin approaches the YCL
792 asters. **(H)** The histogram shows a distinguishable peak, indicating a preferred orientation of the MT bundles
793 in the AV direction.

794

795 VIDEO LEGENDS

796 Video S1. Video shows the three-dimensional render of half embryo with multiple YCL
797 asters, Related to Figure 1.

798 Video S2. Video shows the MTs dynamics of the whole dclk2-GFP embryo during epiboly
799 using Multi-view Light-sheet Fluorescence Microscopy, Related to Figure 2.

Video S3. Video shows an example of the formation of a vortex of MTs in the yolk of a dclk2-GFP embryo with a single YCL aster in the vegetal pole using Scanning Laser Confocal Microscopy, Related to Figure 2.

Video S4. Video shows the formation of a YCL aster in a dclk2-GFP embryo using High Resolution Scanning Laser Confocal Microscopy, Related to Figure 2.

Video S5. Video shows the reabsorption of YCL asters in a dclk2-GFP embryo using High Resolution Scanning Laser Confocal Microscopy, Related to Figure 2.

Video S6. Video shows the reabsorption of YCL asters in a dclk2-GFP embryo using Multi-view Light-sheet Fluorescence Microscopy, Related to Figure 2.

Video S7. Video shows EB3 (red) and MTs (green) dynamics during e-YSN division in a dclk2-GFP embryo using Scanning Laser Confocal Microscopy, Related to Figure 4.

Video S8. Video shows two examples of the animalwards flow and aggregation of centrin puncta in *centrin-gfp* mRNA injected wild type embryos using Multi-view Light-sheet Fluorescence Microscopy, Related to Figure 6.

Video S9. Video shows transmitted infrared (left) and GFP Fluorescence (right) time-lapse images of the YCL asters dynamics containing bright centrin puncta in a *centrin-gfp* mRNA injected wild type embryo using Scanning Laser Confocal Microscopy, Related to Figure 6.

Video S10. Video shows the animalwards flow and aggregation of centin puncta from the YCL and its interaction with e-YSN centrosomes, triggering the e-YSN vegetalwards migration, in *centrin-gfp* mRNA injected wild type embryos using Multi-view Light-sheet Fluorescence Microscopy, Related to Figure 6.

REFERENCES

Andilla, J., Jorand, R., Olarte, O.E., Dufour, A.C., Cazales, M., Montagner, Y.L.E., Ceolato, R., Riviere, N., Olivo-Marin, J.C., Loza-Alvarez, P., et al. (2017). Imaging tissue-mimic with light sheet microscopy: A comparative guideline. Sci. Rep. *7*, 1–14.

Archambault, V., and Pinson, X. (2010). Free centrosomes: Where do they all come from? Fly (Austin). *4*, 172–177.

Bálint, Š., Vilanova, I.V., Álvarez, Á.S., and Lakadamyali, M. (2013). Correlative live-cell and superresolution microscopy reveals cargo transport dynamics at microtubule intersections. Proc. Natl. Acad. Sci. U. S. A. *110*, 3375–3380.

Bartolini, F., and Gundersen, G.G. (2006). Generation of noncentrosomal microtubule arrays. J. Cell Sci. *119*, 4155–4163.

Behrndt, M., Salbreux, G., Campinho, P., Hauschild, R., Oswald, F., Roensch, J., Grill, S.W., and Heisenberg, C.P. (2012). Forces driving epithelial spreading in zebrafish gastrulation. Science. Vol. 338, Issue 6104, pp. 257-260.

Betchaku, T., and Trinkaus, J.P. (1978). Contact relations, surface activity, and cortical microfilaments of marginal cells of the enveloping layer and of the yolk syncytial and yolk cytoplasmic layers of Fundulus before and during epiboly. J. Exp. Zool. Vol 206, issue 3.

Brauchart, J.S., and Grabner, P.J. (2015). Distributing many points on spheres: Minimal energy and designs. J. Complex. *31*, 293–326.

Brodu, V., Baffet, A.D., Le Droguen, P.M., Casanova, J., and Guichet, A. (2010). A developmentally regulated two-step process generates a noncentrosomal microtubule network in Drosophila tracheal cells. Dev. Cell. *18,* 790–801,

Bruce, A.E.E. (2016). Zebrafish epiboly: Spreading thin over the yolk. Dev. Dyn. *245*, 244–258.

Carvalho, L., and Heisenberg, C.P. (2010). The yolk syncytial layer in early zebrafish development. Trends Cell Biol.Vol 20. Nº 10.

Carvalho, L., Stühmer, J., Bois, J.S., Kalaidzidis, Y., Lecaudey, V., and Heisenberg, C.P. (2009). Control of convergent yolk syncytial layer nuclear movement in zebrafish. Development. *136*, 1305–1315.

Cheng, J.C., Miller, A.L., and Webb, S.E. (2004). Organization and function of microfilaments during late epiboly in zebrafish embryos. Dev. Dyn. *231*, 313–323.

Chu, L.T., Fong, S.H., Kondrychyn, I., Loh, S.L., Ye, Z., and Korzh, V. (2012). Yolk syncytial layer formation is a failure of cytokinesis mediated by Rock1 function in the early zebrafish embryo. Biol. Open *1*, 747–753.

D'Amico, L.A., and Cooper, M.S. (2001). Morphogenetic domains in the yolk syncytial layer of axiating zebrafish embryos. Dev. Dyn. *222*, 611–624.

Dammermann, A., and Merdes, A. (2002). Assembly of centrosomal proteins and microtubule organization depends on PCM-1. J. Cell Biol. *159*, 255–266.

872 Eckerle, S., Ringler, M., Lecaudey, V., Nitschke, R., and Driever, W. (2018). Progesterone
873 modulates microtubule dynamics and epiboly progression during zebrafish gastrulation.
874 Dev. Biol. *434*, 249–266.

875 Fei, Z., Bae, K., Parent, S.E., Wan, H., Goodwin, K., Theisen, U., Tanentzapf, G., and Bruce,
876 A.E.E. (2019). A cargo model of yolk syncytial nuclear migration during zebrafish epiboly.
877 Development. *146*, 1–10.

878 Field, C.M., Pelletier, J.F., and Mitchison, T.J. (2019). Disassembly of Actin and Keratin
879 Networks by Aurora B Kinase at the Midplane of Cleaving Xenopus laevis Eggs. Curr. Biol. *29*,
880 1999-2008.e4.

881 Gualda, EJ., Pereira, H., Vale, T., Falcão Estrada, M., Brito, C., and Moreno, M. SPIM-fluid:
882 open source light-sheet based platform for high-throughput imaging. (2015). Biomed. Opt.
883 Express *6*, 4447-4456.
884

885 Hernández-Vega, A., Marsal, M., Pouille, P., Tosi, S., Colombelli, J., Luque, T., Navajas, D.,
886 Pagonabarraga, I., and Martín-Blanco, E. (2017). Polarized cortical tension drives zebrafish
887 epiboly movements. EMBO J.*36,* 25-41.

888 Ishihara, K., Nguyen, P.A., Groen, A.C., Field, C.M., and Mitchison, T.J. (2014). Microtubule
889 nucleation remote from centrosomes may explain how asters span large cells. Proc. Natl.
890 Acad. Sci. U. S. A. *111, 50,* 17715-17722.

891 Ishihara, K., Korolev, K.S., and Mitchison, T.J. (2016). Physical basis of large microtubule
892 aster growth. Elife. *5*, e19145.

893 Jarsch, I.K., Daste, F., and Gallop, J.L. (2016). Membrane curvature in cell biology: An
894 integration of molecular mechanisms. J. Cell Biol. *214*, 375–387.

895 Jesuthasan, S., and Strähle, U. (1997). Dynamic microtubules and specification of the
896 zebrafish embryonic axis. Curr. Biol. *7*,31–42.

897 Juniper, M.P.N., Weiss, M., Platzman, I., Spatz, J.P., and Surrey, T. (2018). Spherical network
898 contraction forms microtubule asters in confinement. Soft Matter *14*, 901–909.

899 Kane, D.A., Warga, R.M., and Kimmel, C.B. (1992). Mitotic domains in the early embryo of
900 the zebrafish. Nature. *360*, 735-737.

901 Kawakami, K. (2007). Tol2: A versatile gene transfer vector in vertebrates. Genome Biol. *8*,
902 1–10.

903 Keating, T.J., Peloquin, J.G., Rodionov, V.I., Momcilovic, D., and Borisy, G.G. (1997).
904 Microtubule release from the centrosome. Proc. Natl. Acad. Sci. U. S. A. *94*, 5078–5083.

905 Kimmel, C.B., and Law, R.D. (1985). Cell lineage of zebrafish blastomeres. II. Formation of
906 the yolk syncytial layer. Dev. Biol.Vol 108, Issue 1, 86-93.

907 Kimmel, C.B., Ballard, W.W., Kimmel, S.R., Ullmann, B., and Schilling, T.F. (1995). Stages of
908 embryonic development of the zebrafish. Dev. Dyn. *203*, 255-310.

909

910 Köppen, M., García Fernández, B., Carvalho, L., Jacinto, A., and Heisenberg, C.P. (2006).
911 Coordinated cell-shape changes control epithelial movement in zebrafish and Drosophila.
912 Development. *133*, 2671-2681.

913 Li-Villarreal, N., Forbes, M.M., Loza, A.J., Chen, J., Ma, T., Helde, K., Moens, C.B., Shin, J.,
914 Sawada, A., Hindes, A.E., et al. (2015). Dachsous1b cadherin regulates actin and microtubule
915 cytoskeleton during early zebrafish embryogenesis. Development. 143(10), 1832.

916 Li, R., and Albertini, D.F. (2013). The road to maturation: Somatic cell interaction and self-
917 organization of the mammalian oocyte. Nat. Rev. Mol. Cell Biol. *14*, 141–152.

918 Lüders, J., and Stearns, T. (2007). Microtubule-organizing centres: A re-evaluation. Nat. Rev.
919 Mol. Cell Biol. *8*, 161–167.

920 Mitchison, T., Wühr, M., Nguyen, P., Ishihara, K., Groen, A., and Field, C.M. (2012). Growth,
921 interaction, and positioning of microtubule asters in extremely large vertebrate embryo
922 cells. Cytoskeleton. *69(10*), 738–750.

923 Montero, J.A., Carvalho, L., Wilsch-Bräuninger, M., Kilian, B., Mustafa, C., and Heisenberg,
924 C.P. (2005). Shield formation at the onset of zebrafish gastrulation. Development *132*, 1187–
925 1198.

926 Moores, C.A., Perderiset, M., Kappeler, C., Kain, S., Drummond, D., Perkins, S.J., Chelly, J.,
927 Cross, R., Houdusse, A., and Francis, F. (2006). Distinct roles of doublecortin modulating the
928 microtubule cytoskeleton. EMBO J. *25*, 4448–4457.

929 Muroyama, A., and Lechler, T. (2017). Microtubule organization, dynamics and functions in
930 differentiated cells. Development. *144*, 3012-3021.

931 Nakamura, M., Masuda, H., Horii, J., Kuma, K.I., Yokoyama, N., Ohba, T., Nishitani, H.,
932 Miyata, T., Tanaka, M., and Nishimoto, T. (1998). When overexpressed, a novel centrosomal
933 protein, RanBPM, causes ectopic microtubule nucleation similar to γ-tubulin. J. Cell Biol.
934 *143*, 1041–1052.

935 Nédélec, F., Surrey, T., and Karsenti, E. (2003). Self-organisation and forces in the
936 microtubule cytoskeleton. Curr. Opin. Cell Biol. *15*, 118–124.

937 Olarte, OE., Andilla, J., Gualda, EJ., and Loza-Alvarez, P. (2018). Light-sheet microscopy: a
938 tutorial. Adv. Opt. Photon. *10*, 111-179.

939 Paoletti, A., Moudjou, M., Paintrand, M., Salisbury, J.L., and Bornens, M. (1996). Most of
940 centrin in animal cells is not centrosome-associated and centrosomal centrin is confined to
941 the distal lumen of centrioles. J. Cell Sci. *109*, 3089–3102.

942 Paz, J., and Lüders, J. (2018). Microtubule-Organizing Centers: Towards a Minimal Parts List.
943 Trends Cell Biol. *Vol 28, Issue 3,* 176-187.

944 Prelich, G. (2012). Gene overexpression: Uses, mechanisms, and interpretation. Genetics
945 *190*, 841–854.

946 Ramkumar, A., Jong, B.Y., and Ori-McKenney, K.M. (2018). ReMAPping the microtubule
947 landscape: How phosphorylation dictates the activities of microtubule-associated proteins.
948 Dev. Dyn. *247*, 138–155.

949 Saff, E.B., and Kuijlaars, A.B.J. (1997). Distributing many points on a sphere. Math. Intell. *19*,
950 5–11.

951 Sánchez-Huertas, C., and Lüders, J. (2015). The augmin connection in the geometry of
952 microtubule networks. Curr. Biol. *25*, R294–R299.

953 Sanchez, A.D., and Feldman, J.L. (2017). Microtubule-organizing centers: from the
954 centrosome to non-centrosomal sites. Curr. Opin. Cell Biol.

955 Sarmah, S., Muralidharan, P., Curtis, C.L., McClintick, J.N., Buente, B.B., Holdgrafer, D.J.,
956 Ogbeifun, O., Olorungbounmi, O.C., Patino, L., Lucas, R., et al. (2013). Ethanol exposure
957 disrupts extraembryonic microtubule cytoskeleton and embryonic blastomere cell adhesion,
958 producing epiboly and gastrulation defects. Biol. Open.*2*, 1013-1021.

959 Schuh, M., and Ellenberg, J. (2007). Self-Organization of MTOCs Replaces Centrosome
960 Function during Acentrosomal Spindle Assembly in Live Mouse Oocytes. Cell. *130*, 484–498

961 Shu, H.B., and Joshi, H.C. (1995). γ-Tubulin can both nucleate microtubule assembly and self-
962 assemble into novel tubular structures in mammalian cells. J. Cell Biol. *130*, 1137–1147.

963 Solinet, S., Mahmud, K., Stewman, S.F., El Kadhi, K. Ben, Decelle, B., Talje, L., Ma, A., Kwok,
964 B.H., and Carreno, S. (2013). The actin-binding ERM protein Moesin binds to and stabilizes
965 microtubules at the cell cortex. J. Cell Biol. *202*, 251–260.

966 Solnica-Krezel, L., and Driever, W. (1994). Microtubule arrays of the zebrafish yolk cell:
967 Organization and function during epiboly. Development. *120*, 2443-2455.

968 Stepanova, T., Slemmer, J., Hoogenraad, C.C., Lansbergen, G., Dortland, B., De Zeeuw, C.I.,
969 Grosveld, F., Van Cappellen, G., Akhmanova, A., and Galjart, N. (2003). Visualization of
970 microtubule growth in cultured neurons via the use of EB3-GFP (end-binding protein 3-
971 green fluorescent protein). J. Neurosci. *23*, 2655–2664.

972 Strahle, U., and Jesuthasan, S. (1993a). Ultraviolet irradiation impairs epiboly in zebrafish
973 embryos: Evidence for a microtubule-dependent mechanism of epiboly. Development *119*,
974 909–919.

975 Teixidó-Travesa, N., Roig, J., and Lüders, J. (2012). The where, when and how of microtubule
976 nucleation - one ring to rule them all. J. Cell Sci. *125*, 4445–4456.

977 Topczewski, J., and Solnica-Krezel, L. (1999). Cytoskeletal dynamics of the zebrafish embryo.
978 Methods Cell Biol. *59*, 205-226.

979 Tran, L.D., Hino, H., Quach, H., Lim, S., Shindo, A., Mimori-Kiyosue, Y., Mione, M., Ueno, N.,
980 Winkler, C., Hibi, M., et al. (2012). Dynamic microtubules at the vegetal cortex predict the
981 embryonic axis in zebrafish. Development. *139*, 3644-3652.

982 Vorobjev, I., Malikov, V., and Rodionov, V. (2001). Self-organization of a radial microtubule
983 array by dynein-dependent nucleation of microtubules. Proc. Natl. Acad. Sci. U. S. A. *98*,
984 10160–10165.

985 Warga, R.M., and Kimmel, C.B. (1990). Cell movements during epiboly and gastrulation in
986 zebrafish. Development. *108*,569-580.

987

988 Wiese, C., and Zheng, Y. (2006). Microtubule nucleation: γ-tubulin and beyond. J. Cell Sci.
989 119, 4143-4153.

990

991 Wu, J., and Akhmanova, A. (2017). Microtubule-Organizing Centers. Annu. Rev. Cell Dev.
992 Biol. 33, 51-75

993

994

995

996

997

998

999

1000

1001

1002

1003

1004

1005

1006

1007

1008

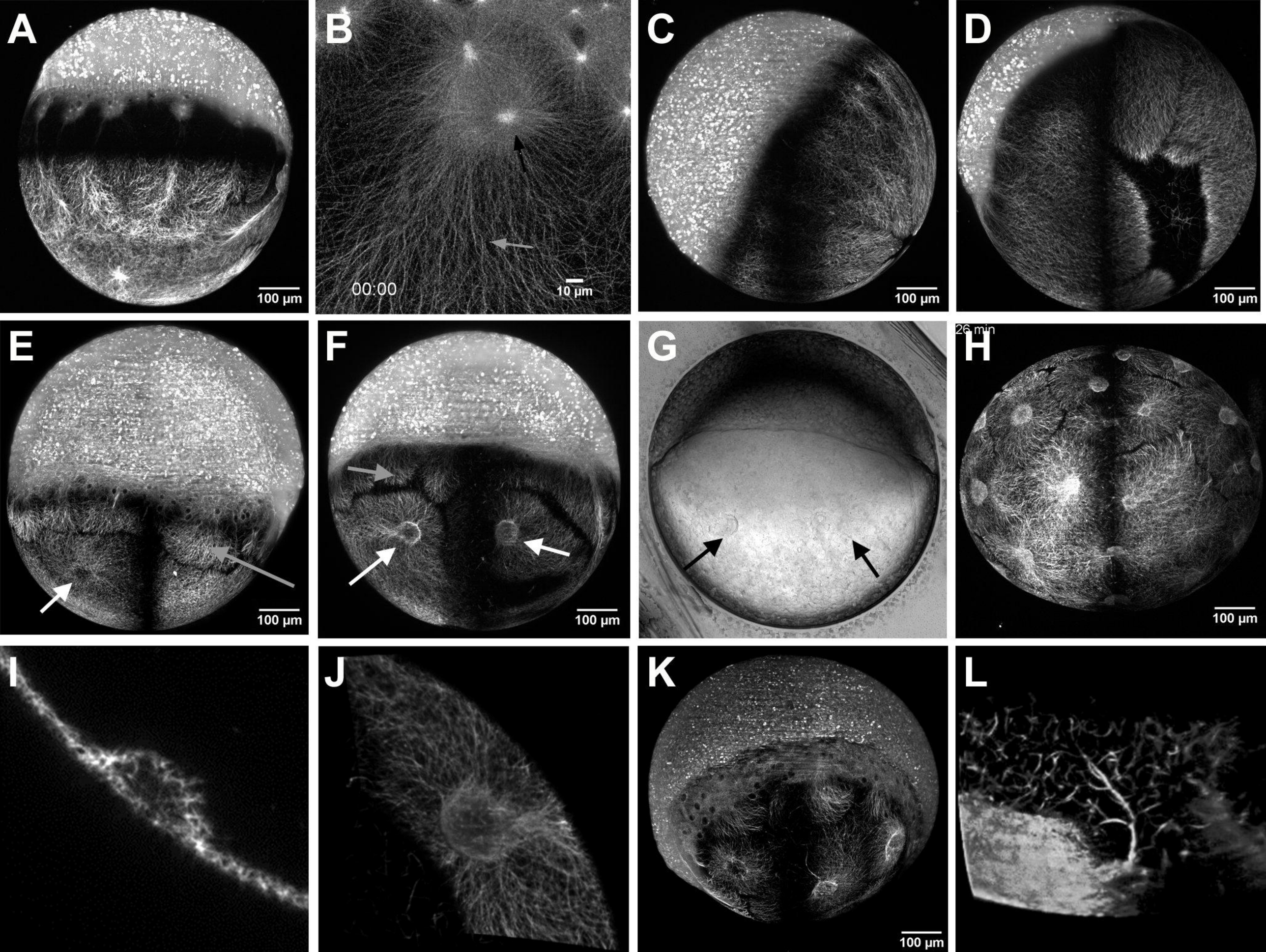
A
100 µm
B
00:00
10 µm
C
100 µm
D
100 µm
E
100 µm
F
100 µm
G
26 min
H
100 µm
I
J
K
100 µm
L

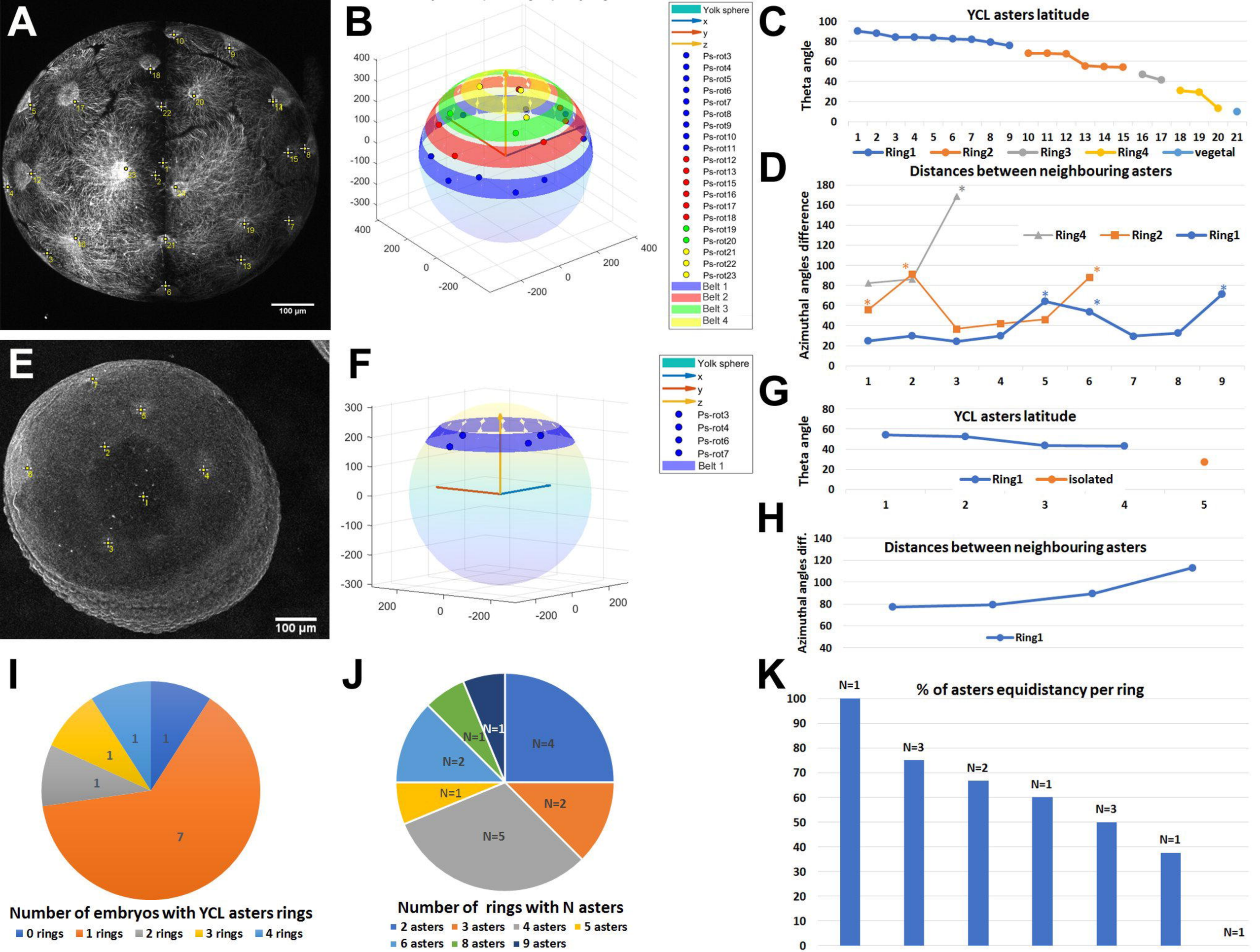
A
100 µm
B
Yolk sphere
x
y
z
Ps-rot3
Ps-rot4
Ps-rot5
Ps-rot6
Ps-rot7
Ps-rot8
Ps-rot9
Ps-rot10
Ps-rot11
Ps-rot12
Ps-rot13
Ps-rot15
Ps-rot16
Ps-rot17
Ps-rot18
Ps-rot19
Ps-rot20
Ps-rot21
Ps-rot22
Ps-rot23
Belt 1
Belt 2
Belt 3
Belt 4
C
YCL asters latitude
Theta angle
Ring1
Ring2
Ring3
Ring4
vegetal
D
Distances between neighbouring asters
Azimuthal angles difference
Ring4
Ring2
Ring1
E
100 µm
F
Yolk sphere
x
y
z
Ps-rot3
Ps-rot4
Ps-rot6
Ps-rot7
Belt 1
G
YCL asters latitude
Theta angle
Ring1
isolated
H
Distances between neighbouring asters
Azimuthal angles diff.
Ring1
I
Number of embryos with YCL asters rings
0 rings
1 rings
2 rings
3 rings
4 rings
J
Number of rings with N asters
2 asters
3 asters
4 asters
5 asters
6 asters
8 asters
9 asters
K
% of asters equidistancy per ring

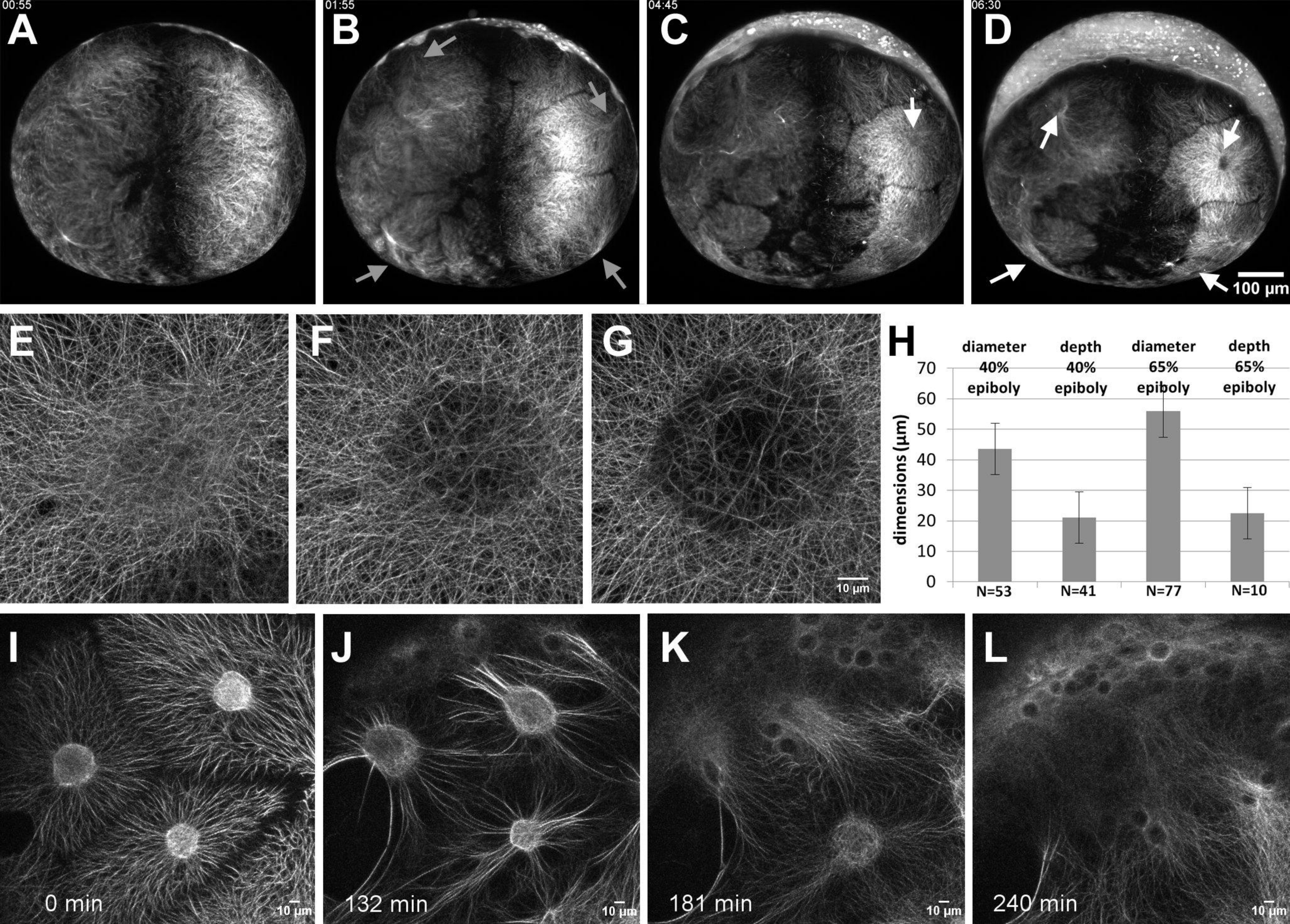
00:55
A
01:55
B
04:45
C
06:30
D
100 µm
E
F
G
10 µm
H
diameter 40% epiboly
depth 40% epiboly
diameter 65% epiboly
depth 65% epiboly
dimensions (µm)
70
60
50
40
30
20
10
0
N=53
N=41
N=77
N=10
I
0 min
10 µm
J
132 min
10 µm
K
181 min
10 µm
L
240 min
10 µm

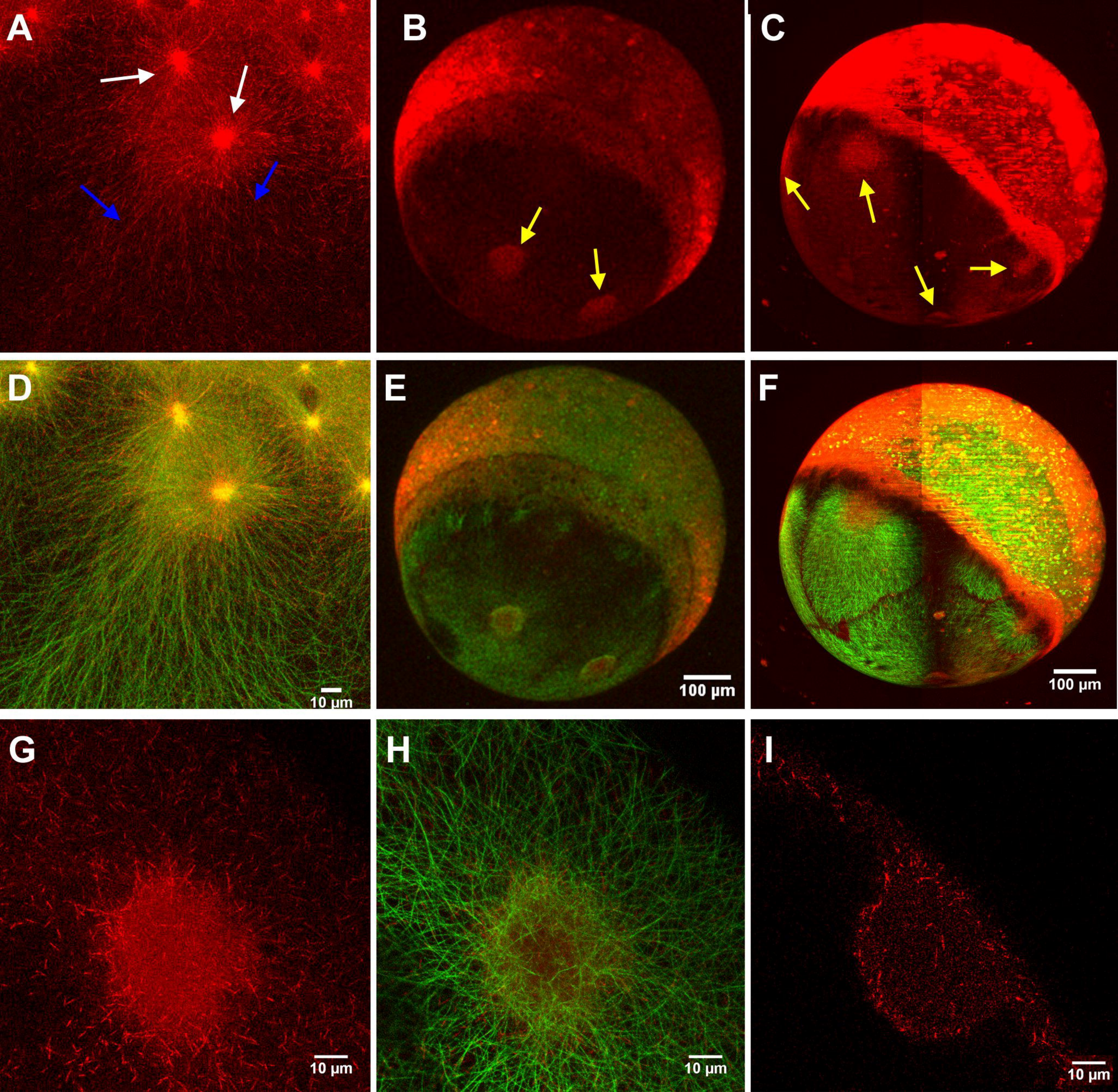
A
B
C
D
10 µm
E
100 µm
F
100 µm
G
10 µm
H
10 µm
I
10 µm

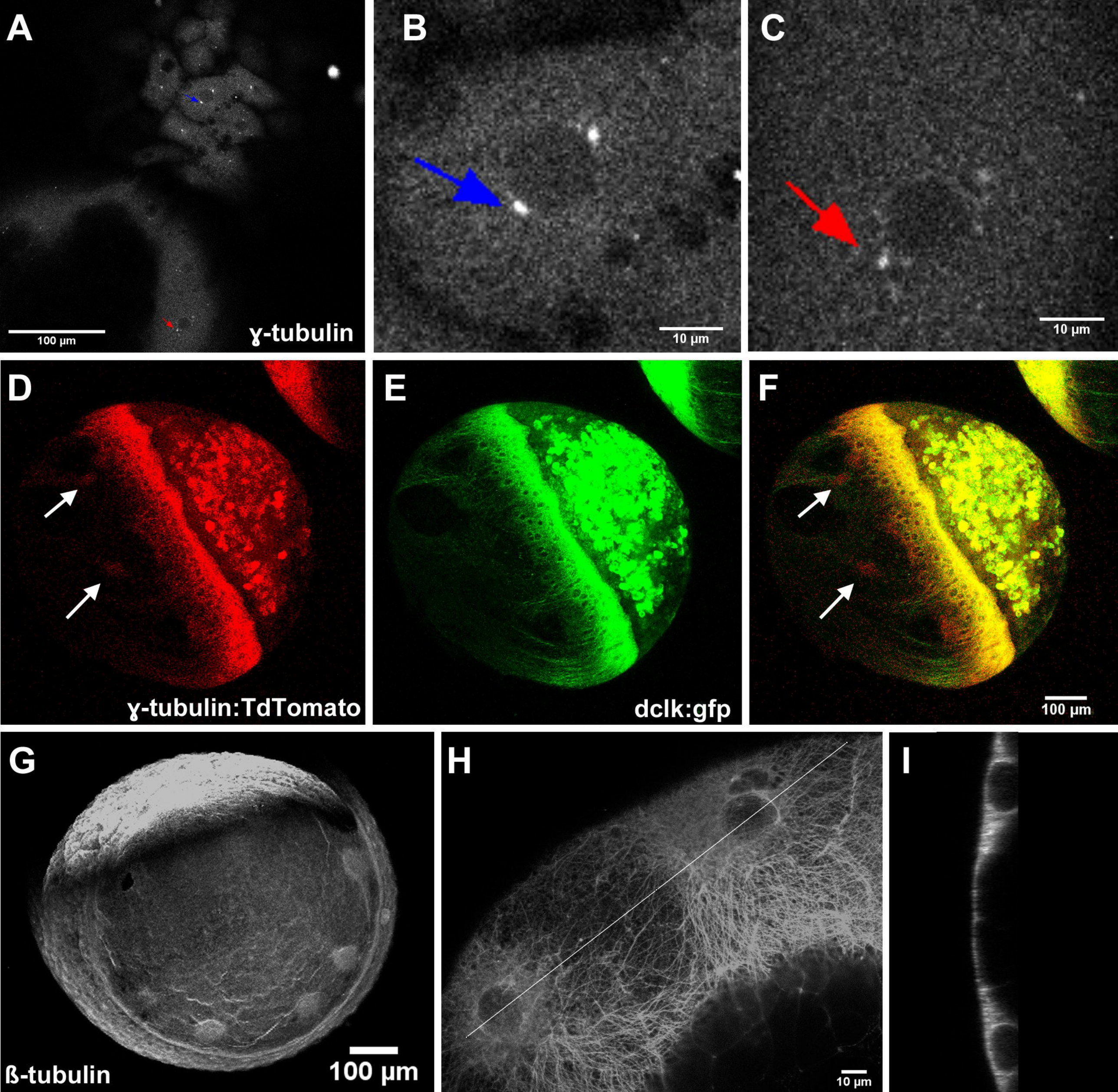
A
100 µm
γ-tubulin
B
10 µm
C
10 µm
D
γ-tubulin:TdTomato
E
dclk:gfp
F
100 µm
G
ß-tubulin
100 µm
H
10 µm
I

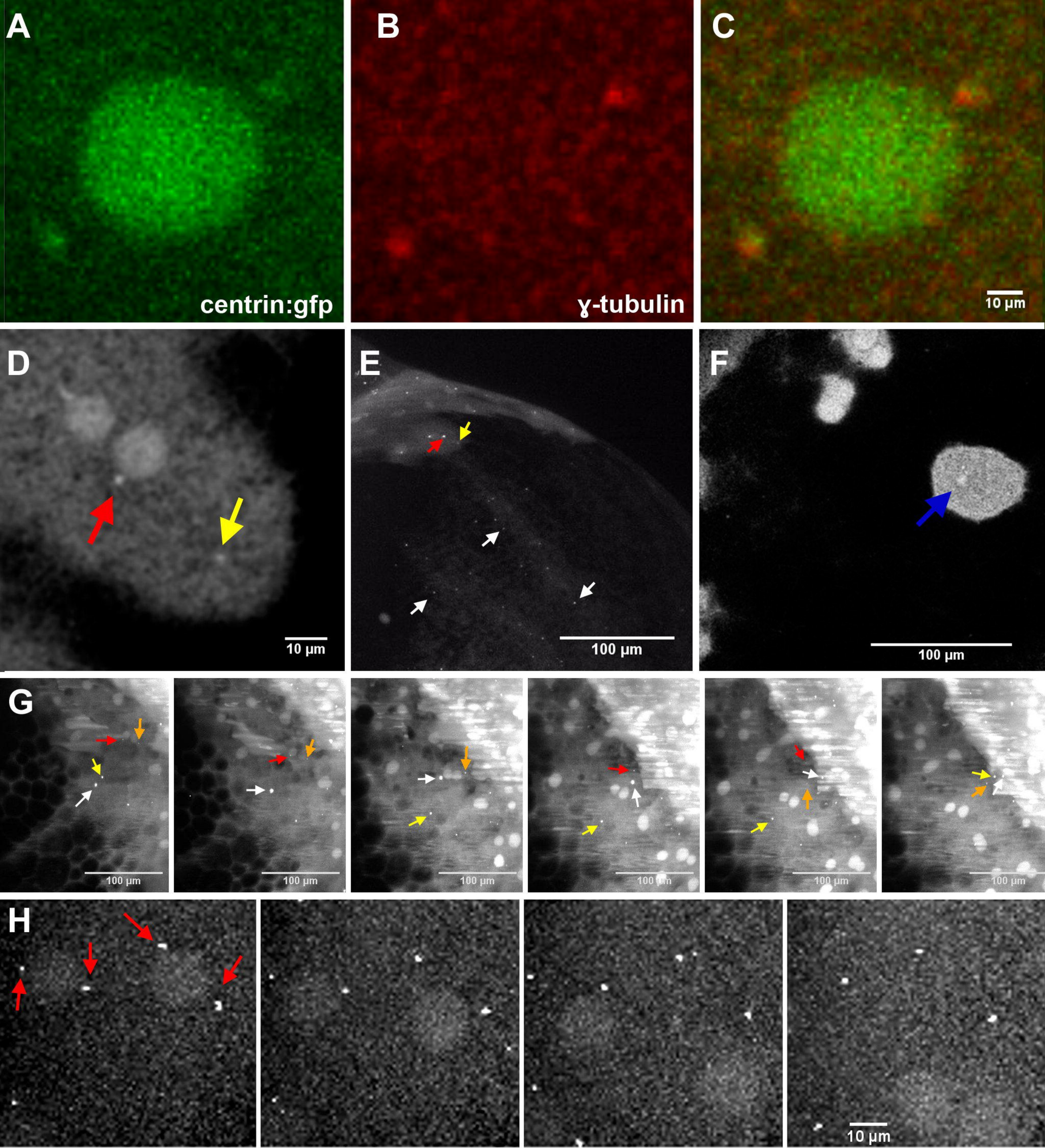
A
centrin:gfp
B
γ-tubulin
C
10 µm
D
10 µm
E
100 µm
F
100 µm
G
100 µm
100 µm
100 µm
100 µm
100 µm
100 µm
100 µm
H
10 µm

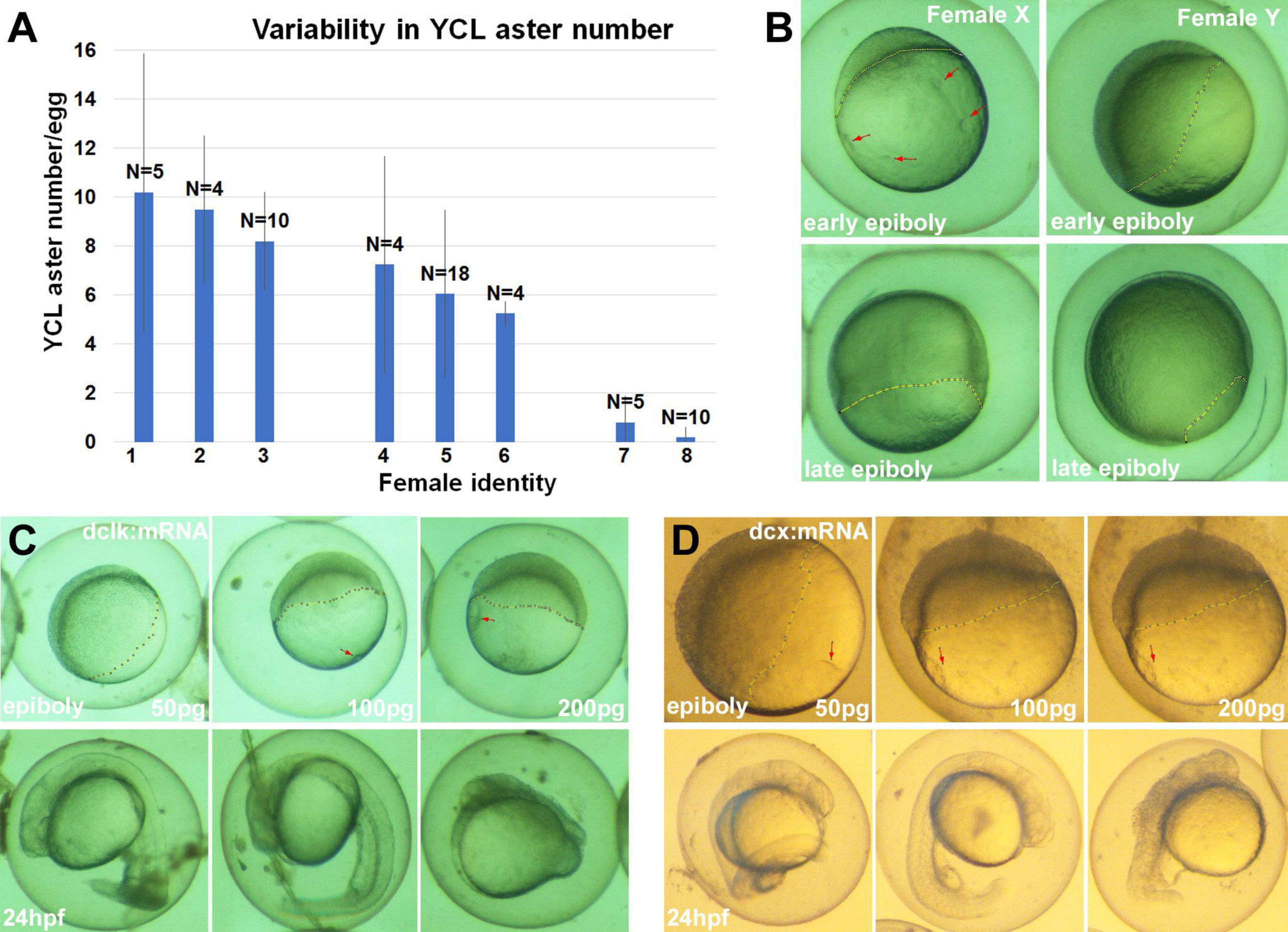
A
Variability in YCL aster number
YCL aster number/egg
16
14
12
10
8
6
4
2
0
N=5
N=4
N=10
N=4
N=18
N=4
N=5
N=10
1
2
3
4
5
6
7
8
Female identity
B
Female X
Female Y
early epiboly
early epiboly
late epiboly
late epiboly
C
dclk:mRNA
epiboly
50pg
100pg
200pg
24hpf
D
dcx:mRNA
epiboly
50pg
100pg
200pg
24hpf